CALIBRATION AND CHARACTERIZATION OF STATIC AND MODULATED OPTICAL TRAPS

by

Yi Deng

B. Sc., Peking University, China, 2003

THESIS SUBMITTED IN PARTIAL FULFILLMENT

OF THE REQUIREMENTS FOR THE DEGREE OF

MASTER OF SCIENCE

IN THE DEPARTMENT

OF

PHYSICS

SIMON FRASER UNIVERSITY

Summer 2007

APPROVAL

Name:	Yi Deng
Degree:	Master of Science
Title of Thesis:	Calibration and characterization of static and modulated optical traps
Examining Committee:	Dr. Karen Kavanagh (Chair)

_____

Dr. Nancy R. Forde, Senior Supervisor

_____

Dr. John Bechhoefer, Supervisor

_____

Dr. Eldon Emberly, Supervisor

_____

Dr. Jeffrey McGuirk, Internal Examiner

Date Approved: June 4, 2007

Abstract

As optical tweezers become widely used in biophysics, calibration becomes essential to quantitatively characterize the dynamics of a system probed by this technique. In this thesis, I apply three methods for calibrating optical tweezers: a direct estimate from thermal motion of a trapped particle using the equipartition theorem, a more advanced approach that analyzes its power spectrum, and a combination of power spectrum analysis and the bead's response under an external driving force. Motivated by recent attempts to use parametric resonance for calibration, I also examine the effects of modulating laser power on the motion of the trapped particle, predicting and finding experimentally an increase in the particle's position variance at low modulation frequencies without evidence for resonant effects in the extremely overdamped motion of the trapped particle. I conclude by discussing future considerations such as the treatment of hydrodynamics and the effect of an anharmonic trap potential.

Acknowledgments

Firstly, I am grateful to my advisor, Dr. Nancy R. Forde for providing me such a great environment for my research, broadening my vision in many areas of science, and building up my confidence in academia. I could not finish this thesis without her help in both science and the thorough corrections in my writing. Thank-you to my thesis committee Dr. John Bechhoefer, Eldon Emberly and my examiner Jeff McGuirk for supervising my project, reading my thesis thoroughly, and sharing ideas and instruments to assist my project.

I thank Philip Johnson for constructing the instrument together with me, as well as Astrid van der Horst and Michelle Lee for discussions in many topics directly and indirectly related to my research. I also thank all members in the Forde Lab for support, and for encouraging me in writing this thesis.

Finally, I would like to warmly thank my dear friends Yang Guo, Zhihao Hao, Shun Lu, Michael Steger, Jeanie Chiu and many others for having great time with me outside the lab during my years of research at Simon Fraser University.

Contents

List of Tables

List of Figures

Chapter 1

Introduction

The fact that light carries momentum has been realized for over a century, but the manipulation of microscopic objects using this momentum was not achieved until two decades ago [1]. However, it only took a few years for this invention, optical tweezers, to find wide applications in physical research, especially in biological systems [2]. In an optical tweezers setup, by control of the momentum exchange between laser light and micron-sized objects, particles like refractive beads and bacteria can be held and moved by the laser light. The applicability of this technique especially to biology is due to the picoNewton force range optical tweezers are able to apply and to their relatively simple setup. In single-molecule studies, optical tweezers are usually used to exert forces on molecules bound to beads, to study the mechanical properties of DNA [3, 4], the unfolding-refolding mechanisms of proteins and DNA and RNA structures [5, 6, 7], the mechanisms of molecular motors [8, 9], and DNA-protein interactions [10, 11, 12], among others. By mechanically inducing conformational changes, it is possible to modify the reaction pathways of biochemical reactions and thus obtain insight into the reaction mechanisms [9, 13]. Molecular motors have been widely studied with optical tweezers, and as such, experimental methodologies have been developed to characterize their properties such as speed, processivity, stall force, and efficiency. Motors that have been studied include myosin [14, 15], kinesin [16, 17], and DNA and RNA polymerases [18, 63]. In cell biology, optical tweezers are widely used to move organelles within the cell [20, 21], or to induce mechanical stimuli to study cell properties such as elasticity and viability [22, 23, 24]. Soft material studies [25], micro-assembly and fabrication [26, 27], particle sorting [28] and artificial lattices [29] have also been studied

using optical tweezers instruments.

To meet the requirements for this wide range of applications, a great variety of optical and mechanical techniques are incorporated in optical tweezers instruments. In order to control the lateral position of the optical trap, the beam path can be manipulated by a rotating mirror [30] or by an acousto-optic modulator (AOM) [31]. Experiments have also demonstrated that rotation of a polarized beam can exert torque on birefringent material or make it rotate [32]. Recent developments in liquid crystal displays make it possible to engineer the wavefront of the light in a real-time fashion. Equipped with these LCD spatial light modulators, dynamic holographic optical tweezers offer three-dimensional control over multiple trapped particles simultaneously [33], while an optical vortex created by holographic optical tweezers provides insight into novel laser modes [34] and is potentially useful in micro-transportation and designing micro-fluidic devices [35]. Other variations on optical trapping include combining it with confocal microscopy [36] and total internal reflection fluorescent microscopy (TIRFM) [14], atomic-force microscopy (AFM) [37], micropipettes, micro surgery techniques [38, 39], fast video imaging [40], and feedback [41] and passive force clamps [42, 43]. These advancements make optical tweezers an extremely flexible and versatile tool with applications in many areas of current research.

Experiments that seek to characterize forces applied to an object require calibration between the optical force and the displacement of the object in the optical tweezers instrument. The relation between force and displacement of a trapped object depends on several parameters: the size, shape, and index of refraction of the trapped particle; the wavelength, beam profile and power of the trapping laser; and the numerical aperture of the focusing objective lens [44, 45]. For small displacements of the trapped particle from its equilibrium position, the particle-trap interaction can be approximated by a harmonic potential characterized by a force-displacement coefficient called the *trap stiffness* or, more loosely, *spring constant*. To determine the trap stiffness experimentally, one can measure directly the displacement produced by a known external force — for example, the Stokes drag in a constant flow [46, 47, 48], or associated with the fluid flow produced by an oscillatory motion of the surrounding solution [47]. An alternate method analyzes the random forces of thermal fluctuations by looking at the variance or the power spectrum of position [44, 49]. While the naive application of such methods produces results that are accurate to $10-20\%$, more refined analyses that consider the hydrodynamics can increase the accuracy ten-fold

[50]. Combining the two methods (viscous drag and power spectrum) eliminates the need to estimate the hydrodynamic drag coefficient or equivalently the size of the particle, a persistent potential source of systematic error [49]. In the first part of this thesis, I describe the implementation of these calibration techniques in our optical tweezers instrument.

Recently, Joykutty *et al.* attempted to develop a new method for calibrating the stiffness of an optical trap that was based on the periodic modulation of trap stiffness [51]. While there are serious difficulties with that technique [52, 53], the effects of a modulated trap have both fundamental and practical interest, and I focus on these aspects in the second part of this thesis.

In an underdamped mechanical system, periodic temporal modulation of trap stiffness can lead to parametric resonance [54]. The Brownian motion of atoms in magneto-optical traps (another type of optical trap) has been studied both theoretically [55] and experimentally [56, 57]. Under the proper conditions, trap modulation can lead to an increase in damping and a decrease in the variance of positional fluctuations of the Brownian particle. Such a decrease corresponds to a cooling of the temperature of the trapped particle and is a desired feature of such traps. On the other hand, parametric excitation can also lead to an instability (Hopf bifurcation), where the motion of the particle increases exponentially – an undesirable result [58]. Thus, a full understanding of the effects of modulation is important in such cases.

In optical trapping in aqueous media, the motion is extremely overdamped, with dimensionless dampings that are typically $\mathcal{O}(10)$. (The dimensionless damping is proportional to the ratio of the natural oscillation period of the particle to its relaxation time in the viscous fluid, and is one for a critically damped system.) As we shall see, in the overdamped limit, parametric modulation does not lead to the resonant effects seen in underdamped systems; however, in the low-frequency limit, I will show that modulation does increase the variance of the particle's position. There are practical consequences to this effect, as there are a number of situations of recent interest where the trap stiffness is indeed modulated. For example, in time-sharing optical traps, the direction of the trapping beam is switched among several angles to create multiple traps [48]. For each trap, the power turns on and off periodically, a temporal modulation. In another example, linear-scanning optical tweezers [43] create a constant force optically. In this technique, the potential is modulated both spatially and temporally. In all these cases, the increase in position variance produced by modulation

is an undesired effect. While simple arguments show that modulating the trap strength at frequencies greater than the particle's response frequency ensures that its stiffness may be safely approximated by its time-averaged value [48], the work described in the second part of this thesis investigates experimentally and theoretically the consequences of modulating at a lower frequency.

Specifically, in my thesis, I first introduce the detailed setup of our optical tweezers instrument, then present multiple calibration methods using the bead's thermal motion including the basic equipartition theorem method, power spectrum analysis of the Brownian motion in a stationary optical trap and preliminary results for a hybrid method probing the power spectrum of a trapped particle subjected to external spatial perturbation. In Chapter 3, I experimentally measure the variance of the position of the trapped object in a temporally modulated optical trap and compare the result with the predictions of a simple theory based on the overdamped Brownian motion of a particle in a parametrically modulated harmonic trap. A null-test of the parametric resonance is finally presented to show that parametric resonance is neither expected nor observed in an overdamped system.

Chapter 2

Building and calibrating the optical tweezers

Quantitative characterization of the optical trap is important for studying systems using this technique. In this chapter, I briefly describe the principle of optical trapping, then outline the specific instrumental setup of our optical tweezers, and finally introduce multiple methods for trap calibration, which involves finding the relation between the optical force and the displacement of a trapped particle.

2.1 Principles of optical trapping

Optical tweezers involve an object interacting with light and can be described in terms of momentum exchange between the trapped object and the light field holding it in place. When light interacts with a particle, its momentum is altered and the Poynting vector of the light field, defined as the energy flux, which is also proportional to the momentum density, changes its direction. This interaction gives rise to an optical force and has been known for a long time. This effect was first applied to generate optical trapping by Arthur Ashkin [1].

A simplified version of the trapping principle can be stated using ray optics, as follows: If a dielectric spherical object is placed on the centre line of a Gaussian beam, it will experience no net force on its lateral direction due to symmetry (Figure 2.1 (a)). When the object is off-centered, the mismatch in the intensity of light being refracted by the object

near and far from the centre line creates a net momentum change for the bead that has a lateral component pointing towards the centre of the beam, or equivalently along the gradient of the light intensity (Figure 2.1 (b)). This component is called the *gradient force*.

In this picture, the change in light momentum also has an axial component which causes a "downstream" force on the object. In addition, reflections on the interfaces generate force that has a similar effect. These downstream forces and components all together are called the *scattering force* (Figure 2.1 (a)).

For trapping in three dimensions, a gradient in the axial direction is created by tightly focusing the beam, thus creating a gradient force strong enough to overcome the scattering force (Figure 2.1 (c), (d)). Experimentally, a laser and a high numerical aperture (NA) microscope objective lens are commonly used to create a strong gradient in the axial direction.

To estimate the trap stiffness, it is useful to consider the trapped dielectric particle as a electric dipole. For a linear dielectric material, the polarization density $\mathbf{p}$ is related to the electric field $\mathbf{E}$ as[1]

$$\mathbf{p} = \alpha \mathbf{E} \,. \tag{2.1}$$

Here α is the polarizability of the trapped particle. For a dielectric sphere of radius R [44, 59],

$$\alpha = n_m^2 \epsilon_0 \left(\frac{m^2 - 1}{m^2 + 2} \right) R^3 \,, \tag{2.2}$$

where ϵ_0 is the permittivity of free space, and $m \equiv \frac{n_p}{n_m}$ is the ratio between the index of refraction of the particle n_p and the medium n_m.

The time-averaged gradient force $\mathbf{F}$ of an electric dipole in an inhomogeneous light intensity I is

$$\mathbf{F} = \frac{\alpha}{4\epsilon_0 c n_m^2} \nabla I \,. \tag{2.3}$$

At the focal point of the microscope objective, we approximate the focused light as a planar wave with a Gaussian intensity profile perpendicular to the optical axis, with a width of one wavelength λ:

$$I(r) \approx \frac{P}{\pi \lambda^2} e^{-r^2/\lambda^2} \,, \tag{2.4}$$

where r is the distance from the optical axis, and P is the total power of the laser at the focal area.

[1] The estimation is shown in MKSA units.

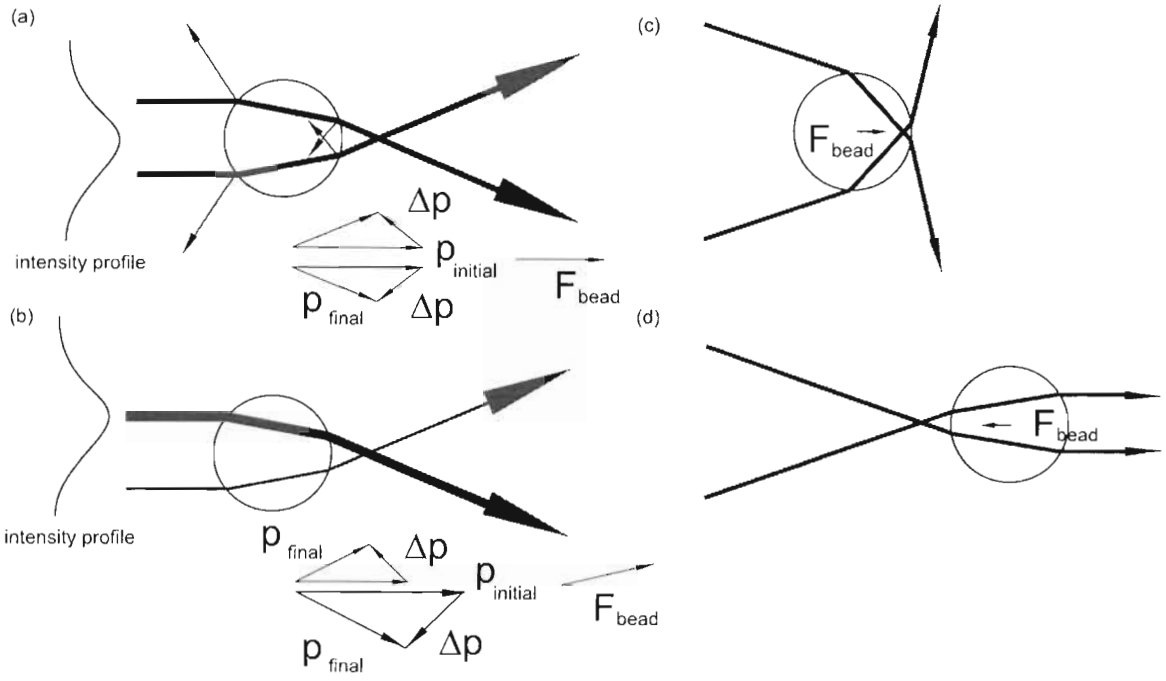

Figure 2.1: Principle of optical trapping illustrated by ray optics. (a) Refraction of light by a bead on the centre line of a collimated beam. The refracted light has a symmetric distribution in the lateral direction, but its momentum is reduced in the downstream direction. The thin arrows show the reflected light that also contributes to the downstream scattering force. Reflections are omitted in (b), (c) and (d). (b) When the bead is off-centred, the intensity asymmetry in the lateral direction causes a net force on the bead with a component along the gradient of the light intensity. (c) In the focused light of a 3-D trap, when the bead is upstream of the focus, the total force pushes the bead downstream. (d) The downstream bead will experience force that pulls it back towards the beam focus.

The trap stiffness at the centre on the perpendicular direction to the optical axis is

$$\begin{aligned} \kappa_{\perp} &= |\frac{\partial}{\partial r}\mathbf{F}(\mathbf{0})| \\ &= \frac{R^3 P}{2\pi c \lambda^4}\left(\frac{m^2-1}{m^2+2}\right) . \end{aligned} \tag{2.5}$$

This expression only applies to particles much smaller than the wavelength. Nonetheless, it can be extended to larger dielectric particles to estimate the trap stiffness. Assume a 3 μm-diameter polystyrene bead is trapped by a 100 mW, 800 nm-wavelength laser. The indices of refraction of water and polystyrene are taken as 1.33 and 1.59. The trap stiffness is then $\sim 10^2$ pN/μm. This very crude attempt does not agree with experimental observations. Nonetheless, it illustrates the cause of the gradient force, and gives a order-of-magnitude estimation of the trap stiffness. The physical picture of a trapped particle that has comparable size with the wavelength is more complicated. The ray diagram picture, Rayleigh scattering approach and the treatment based on Mie scattering theory have been attempted to theoretically calculate the optical forces with different levels of success. [45, 60, 61]. This thesis will not discuss these theoretical works any further, but instead will focus on the trap calibration by experimental means.

2.2 Description of the instrumentation

Optical tweezers are commonly built on a commercial inverted microscope, or from basic optical elements and microscope objectives. For a commercial microscope, the alignment is easier, and there is a set of microscope accessories available. Customized optical tweezers, however, have more flexibility in their optical configuration. In our lab, we built the optical tweezers following the latter scheme. For ease of description, our optical tweezers system is divided into several components: optics for trapping, position detection and electronics, pressure control and fluidic system (Figure 2.2).

2.2.1 Trapping optics

Our optical tweezers setup is a position-measuring optical tweezers with a single trap (Figure 2.2). The 835 nm light from a 200 mW diode laser (diode from JDS Uniphase FG5431-

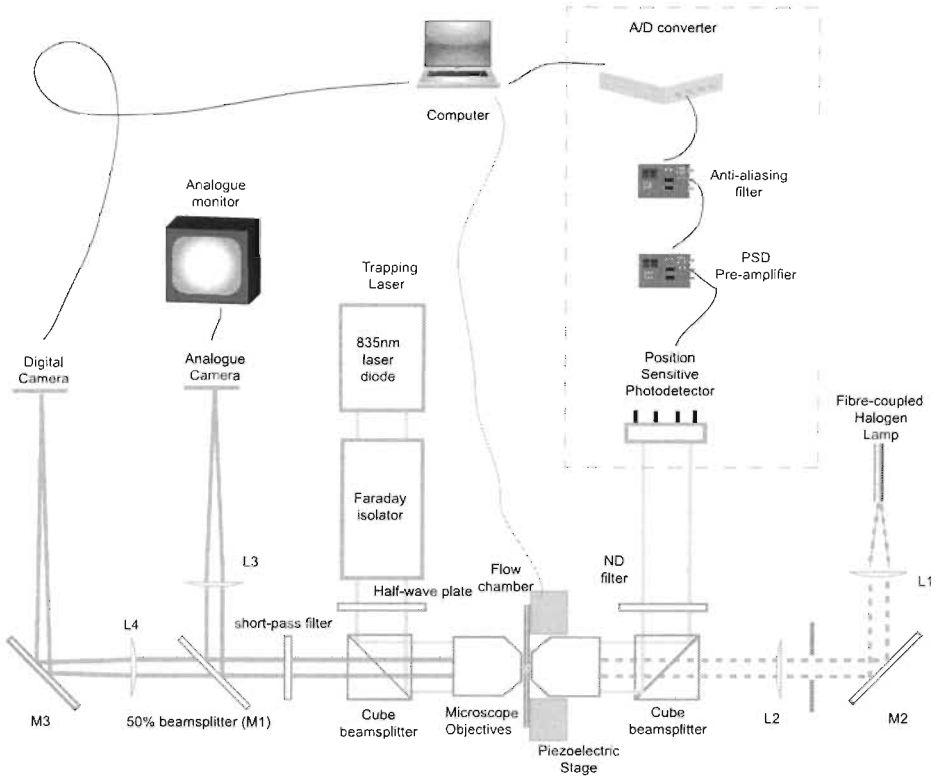

Figure 2.2: Schematic layout of the optical tweezers setup. A 200 mW, 835 nm near-infrared diode laser is used as the trapping laser source. The collimated laser beam is sent to and focused by a high-NA microscope objective to create an intensity gradient for trapping. On the downstream side an identical objective is used to collect and recollimate the transmitted (forward-scattered) light for position detection on a lateral effect position-sensitive photodetector (PSD). A halogen lamp is placed on the condenser side as the illumination light source, and the image is split by a 50% beam splitter for imaging on two cameras, one analogue and the other digital. For ease of viewing, the illumination beam path indicated in green lines is simplified from Köhler illumination in the actual setup. The detailed alignment procedure is described in Appendix D. The flow chamber in which the laser light is focused is mounted on a computer-controlled piezoelectric stage, enabling relative motion between two beads for biological studies. The dashed square indicates the parts for position detecting: PSD, PSD pre-amplifier electronics, anti-aliasing filter and A/D converter. The flow control system for the trapping chamber is omitted in this drawing. Abbreviations used here are: L=lens; M=mirror; ND=neutral density. See [62] for more details. The focal length of the lenses are: L1 - 40 mm, L2 - 50 mm, L3 - 150 mm, and L4 - 500 mm. The cube beamsplitter we use is 03 PBS 065, Melles Griot.

G1-830-10-G1-.2; laser assembled by Melles Griot) is focused by an objective lens (Olympus UPlanApo/IR, NA 1.2, 60X, water immersion) into a flow chamber to trap polystyrene beads (Spherotech). A Faraday isolator (Optics for Research Inc., IO-10-834-LP) protects the laser from back-scattered light. The transmitted (forward-scattered) light is collected by an identical objective lens. The position of the trapped bead can be obtained from analysis of the displacement of the laser beam on a position-sensitive photodetector (PSD, UDT Sensors DL-10). On the downstream side, fibre-coupled halogen lamp (Dolan-Jenner Industries, Inc., Series 180) is used as the illumination light source. The image of the trapped bead is sent to two cameras, one analogue with a small magnification for an overview of a large area, and the other a digital CCD camera (Flea, Point Grey) capturing the image which is sent to a computer for image analysis. The whole setup is enclosed in a plastic shield to reduce laser-beam deflection due to air currents [63]. See Appendix D for a brief instruction on optical alignment.

2.2.2 Pressure control and fluidic system

For biophysical experiments, a flow control system is incorporated in the optical tweezers setup. We make the flow chamber and chamber holder in our lab following Steven Smith's design [3]. The chamber is made of two pieces of cover glass separated by melted Nescofilm (Karlan Research Products Corp.) with chamber-shaped cuts. A piece of polymeric tubing (Microfil34G, World Precision Instruments) is placed in the middle of the chamber for pipette insertion. One of the cover glasses has holes drilled to connect with silicon tubes (Figure 2.3).

The flow speed at the injection side of the flow chamber is set by applying pressure. Pressure is regulated by three valves controlled by the computer, connecting with compressed nitrogen from a shared pipeline, a vacuum aspirator and atmosphere. Between the pressure sources and the flow chamber, a computer-controlled valve selector is inserted to switch among up to four solution reservoirs [62].

The flow chamber is mounted in a chamber holder, which is attached to a piezoelectric stage (Mad City Labs, NANO-H50) by four magnets. The stage is able to move 50 μm in two directions with sub-nanometer resolution. The pipette mounted on the stage therefore can be moved relative to the fixed optical trap. In this setup, molecule stretching exper-

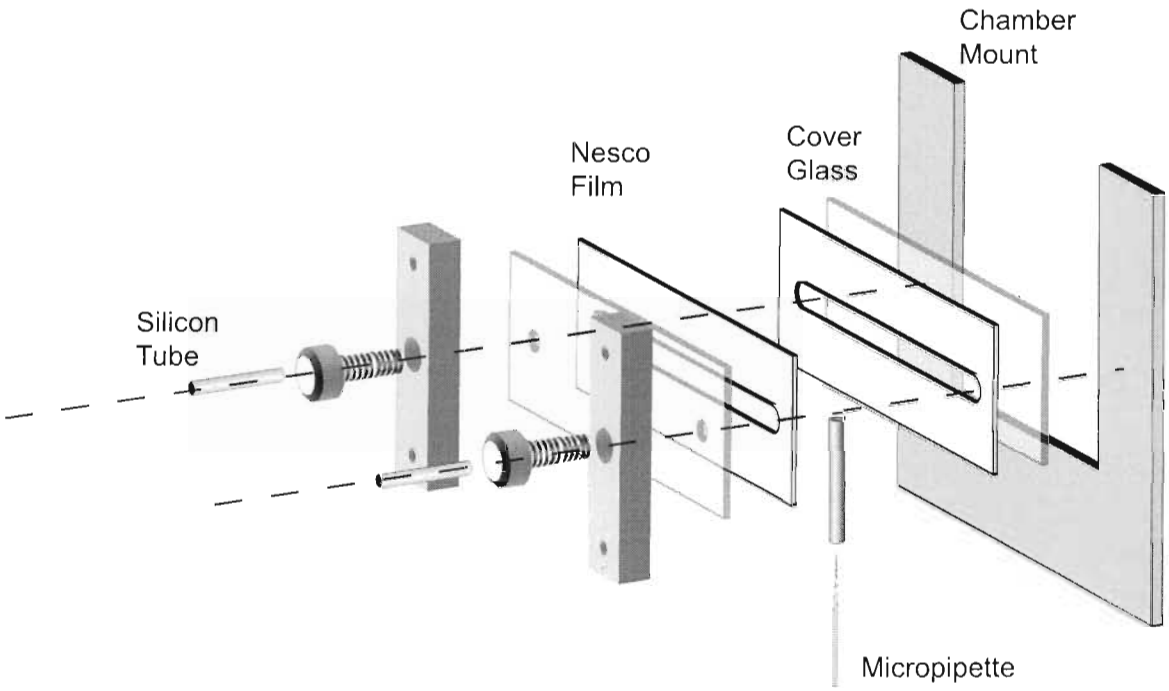

Figure 2.3: Design of the flow chamber. The chamber is made of two pieces of Nescofilm and two pieces of cover glass, one of which has drilled holes for fluid exchange. On one side of the chamber, a piece of polymeric tubing is placed between the Nescofilm so that micropipette is easily inserted and replaced.

iments and studies on molecular motors are possible, by tethering the sample between a bead held on the micropipette by suction and a bead held in the optical trap.

For details on procedures of making chambers and micropipettes, pressure regulation and flow speed control, see [62].

2.2.3 Position measurement

The position of the bead is measured in two ways. In one method, the image of the bead is acquired by a CCD camera, and the image is analyzed in software for edge detection to find the centroid of the bead [62]. In this method the position is determined to sub-pixel resolution (10 nm of the position signal for a fixed bead of 0.2 pixel from the tracking algorithm[2]), and this method can analyze several beads simultaneously. The main limitation is the frame rate of the camera, and the computational burden. In this setup, the camera is able to run at 640×480 pixel resolution, 8 bit grey scale at 60 frames per second. Therefore the detection bandwidth of the bead position is limited to 60 Hz. In many biological systems, this rate is fast enough to track major dynamical events, but it is unable to completely characterize the Brownian motion of the bead in the trap, which can be essential in some high-precision measurements [63]. Fast cameras are commercially available; however, images must be recorded for later analysis as real-time analysis is limited by the data transmission rate and computation power of the computer.

Another way to determine the bead's position is to collect information in the laser light after it interacts with the bead, using a position-sensitive photodetector (PSD). Both back-scattered light and transmitted light can be used for measuring the position. Over a certain range, the centre of the transmitted light is proportional to the position of the bead relative to the trap centre. The straightforward picture is that the momentum change of the light caused by the bead is described by the angular redistribution of the light intensity, which is then transformed into the spatial profile of the light by the condenser objective. Therefore the shift of the centre of the recollimated light indicates the momentum change of light per unit time induced by the bead. In our setup, we use a lateral-effect position-sensitive photodetector to measure the position of the centre of the light, and thus the position of the

[2]Estimated from the magnification of the camera of 22 pixel/μm and the standard deviation of the position signal for a fixed bead of 0.2 pixel.

trapped bead, since the bead displacement is proportional to the optical force over a small range. The signal is amplified by an analogue amplifier, low-pass filtered for anti-aliasing (LTC1064-2CN, Linear Tech), sampled by an A/D converter (PCI-6052E, National Instruments) and sent to the computer for processing. The position-measurement bandwidth is limited by the response of the photodetector (8 MHz, for 650 nm light, according to the manufacturer), the amplifier (300 kHz, see detailed discussions below), and the A/D converter (typically 50-100 kHz, set by the sampling frequency). This bandwidth is sufficiently high for calibrating our optical tweezers as described below.

Other approaches to position measurement have been introduced in the literature [44]. In our setup, video microscopy and the forward-light scattering measurement are precise and fast enough for basic physical and biological studies.

2.2.4 Position calibration

In order to obtain the position of the trapped bead in "real" units (e. g. μm), the signals from PSD voltage and particle tracking from video microscopy must be calibrated. In this procedure, I fixed a bead on the pipette tip and moved it around the trapping area. The movement of the piezoelectric stage is taken as the displacement standard, since the stage is calibrated to sub-nanometer precision by the manufacturer. At the same time, the response of the PSD and video tracking results are recorded.

In order to obtain the conversion factors with high signal-to-noise ratio on both horizontal and vertical directions, I moved the pipette in diagonal scan instead of a 2-D line scan to avoid drift occurring over the timescale of a full x-y scan. A 3.1 μm-bead was moved through the trap area on a diagonal line, with a scan rate of 5 Hz across 0.5 μm in each direction. The voltage signal of the PSD on both channels and the position sensor voltages on the piezoelectric stage are sampled at 1200 Hz and averaged over 20 samples to give a 60 Hz effective sampling rate. The coordinates of the bead centre given by video tracking are determined at 30 frames per second. The resultant video tracking position and PSD voltage are plotted against the stage movement in Figure 2.4. The video magnification is determined to be 22.11$\pm$0.07 pixel/μm and 22.33$\pm$0.06 pixel/μm for the horizontal and vertical directions respectively, and respectively the PSD magnification is 0.9526$\pm$0.0008 V/μm and 1.1716$\pm$0.0005 V/μm for the two directions. The difference between PSD con-

version factors in the two directions may result from the optical alignment, the sensitivity of the PSD, and/or the different channel amplifications of the PSD pre-amplifier[3]. Also note that the PSD magnifications in both directions depend on the specific size of the trapped bead, as shown in the following sections.

I also attempted to correlate the video tracking result with the PSD voltage signal for an optically trapped bead. However, because the coherence time of the bead position is on the scale of milliseconds[4], it is technically hard to synchronize the video frames and the PSD voltage signal. In addition, the integration time of the CCD camera will cause problems in determining the instantaneous position of the bead. Also because this correlation measurement does not give further information than the moving-pipette measurement for calibrating the magnifications, I did not investigate this method further.

2.3 Trap calibration using Brownian motion

One way to calibrate the trap is to apply directly an external force using a known constant flow, and observe the displacement of a trapped bead [47, 62]. Another category of techniques for calibrating the trap stiffness uses thermal motion of the trapped bead; these include the equipartition method, the power spectrum method and some variations. The power-spectrum method is found to be the best method, as it is a quick and relatively accurate way to calibrate the trap stiffness. These approaches are described below.

This section contains the main trap calibration procedure using the bead's thermal motion and results. Sections 2.3.1 and 2.3.2 introduce the theoretical background for calibrating, followed by Section 2.3.3 where the hydrodynamic effects are considered for corrections to the power spectrum method. Two technique sections, Sections 2.3.4 and 2.3.5, introduce two data-compression treatments and the details of setting up the anti-aliasing scheme. The results are listed and discussed in Section 2.3.6. Section 2.3.7 discusses the correlation of the thermal motion between the horizontal and vertical directions and the

[3]The amplification of the DL-10 pre-amplifier is measured using a variable dummy load, showing a 1:1.1 ratio on the two channels of the amplifier (data not shown). This difference results from unmatched resistances in the amplifier.

[4]The coherence time is the reciprocal of the corner frequency, which is around 1 kHz for a 2 μm bead in a 100 pN/μm trap. See section 2.3.2 for a description of the corner frequency.

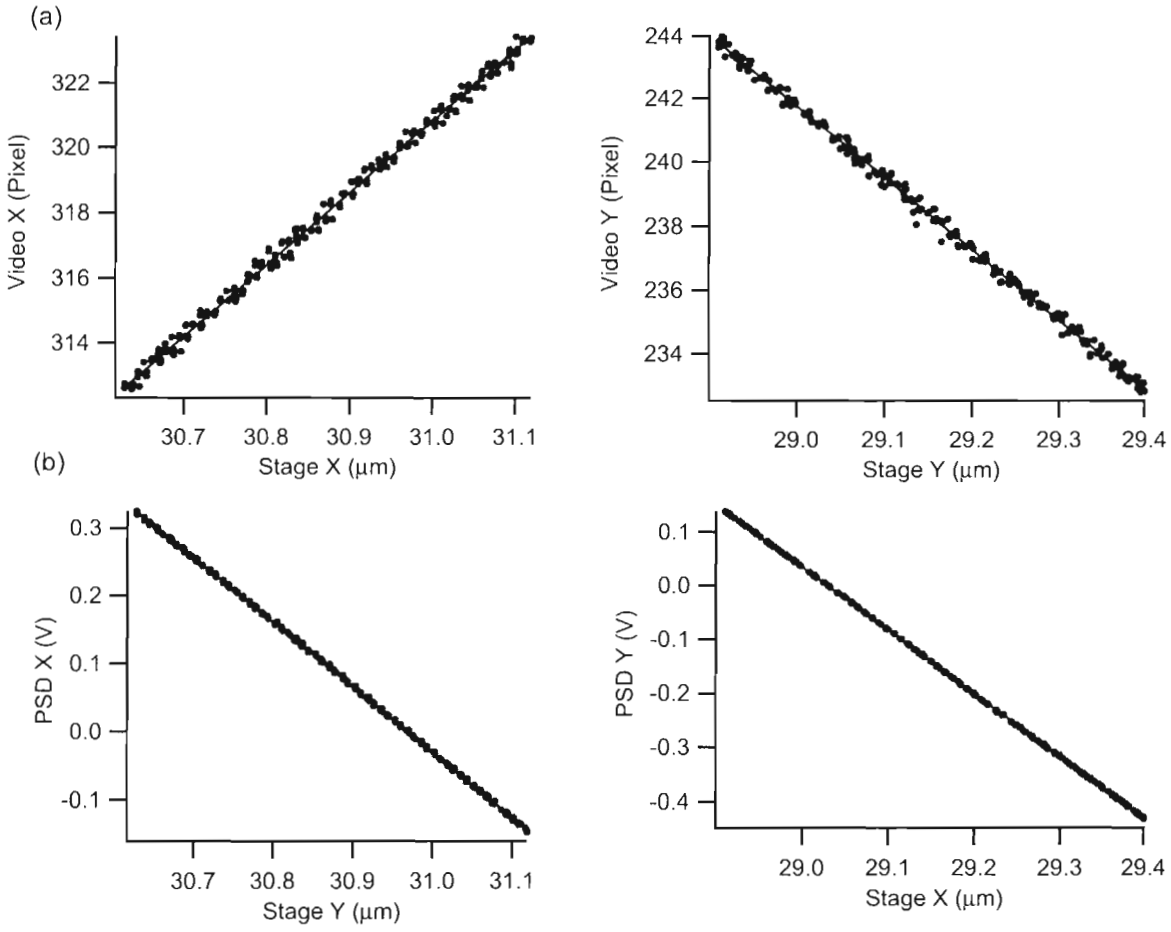

Figure 2.4: Calibration of the video microscopy and PSD position detection magnification of a 3.1 μm bead fixed on the pipette tip. (a) The video magnifications are determined as 22.11$\pm$0.07 pixel/μm and 22.33$\pm$0.06 pixel/μm for the horizontal and vertical directions respectively. (b) The PSD magnifications are 0.9526$\pm$0.0008 V/μm and 1.1716$\pm$0.0005 V/μm for the two directions. The video magnification only depends on the magnification of the trapping objective and the focal length of the imaging lens, whereas the PSD magnification depends on the collimation, the size of the trapped object and the sensitivity of the photodetector.

possible reasons for the non-zero correlation. Most of the work in this section follows Berg-Sørensen and Flyvbjerg's work on calibrating an optical trap [50].

2.3.1 Position variance and the equipartition theorem method

According to the equipartition theorem, the variance of a trapped bead is related to the thermal energy by

$$\frac{1}{2}\kappa\langle x^2\rangle = \frac{1}{2}k_BT\,, \tag{2.6}$$

where $\frac{1}{2}k_BT$ is the thermal energy in one spatial dimension, and the left hand side is the average potential energy of a bead in a harmonic trap of stiffness κ.

As stated above, the bead's position is measured by the photodetector, therefore the conversion factor from voltage to real displacement must be obtained in order to determine the trap stiffness in force per real length units. Thus this conversion factor is a direct source of error.

2.3.2 Basic Lorentzian form of the power spectrum

The equipartition theorem uses the thermal energy of the trapped bead to evaluate the strength of the trap. However, the overall variance of the position neglects all the detailed motion information, specifically the energy distribution of each frequency component of motion, which is related to the structure of the trapping potential.

In our optical trap, the interaction between the laser and the trapped object can be approximated by a harmonic potential. In such a case, the equation of motion for the trapped bead is given by the Langevin equation,

$$m\ddot{x} - F_{drag} + \kappa x = \sqrt{2k_BT\gamma_0}\,\xi(t)\,. \tag{2.7}$$

Here, m is the mass of the bead, x its position, κ the trap stiffness, F_{drag} is the drag force on the bead, k_BT the thermal energy and $\xi(t)$ is a stochastic Gaussian process satisfying

$$\langle\xi(t)\rangle = 0\,; \tag{2.8a}$$

$$\langle\xi(t)\xi(t')\rangle = \delta(t-t')\,. \tag{2.8b}$$

For a spherical object with radius R, the drag force term in a laminar flow is calculated as

$$F_{drag} = -\gamma_0 \dot{x} \,, \tag{2.9}$$

where the drag coefficient γ_0 is well approximated by a constant determined by Stokes' law,

$$\gamma_0 = 6\pi\rho\nu R \,, \tag{2.10}$$

where ρ is the density of the surrounding fluid, ν its kinematic viscosity and R the radius of the spherical object. In an optical trap, the bead is driven by thermal forces and therefore moves with a variable velocity. The actual drag force has a more complicated relation than (2.9) and (2.10), as discussed in the next section. Here, I will start with the simple expression without any consideration of hydrodynamical effects.

Since a micron-sized bead optically trapped in an aqueous environment is a highly over-damped system, the inertial term can be dropped from (2.7), leaving

$$\gamma_0 \dot{x} + \kappa x = \sqrt{2k_B T \gamma_0}\,\xi(t) \,. \tag{2.11}$$

Applying a discrete Fourier transform to both sides, we have[5]

$$2\pi i f_k \gamma_0 \tilde{x}_k + \kappa \tilde{x}_k = \sqrt{2k_B T \gamma_0}\,\tilde{\xi}_k \,, \tag{2.12}$$

or

$$\tilde{x}_k = \frac{\sqrt{2k_B T \gamma_0}\,\tilde{\xi}_k}{2\pi i f_k \gamma_0 + \kappa} \tag{2.13}$$

Symbols with tildes on top represent the Fourier transforms of the corresponding variables with frequency index k, when measured for finite length T_{msr} (Appendix A.1). It can be shown from Wiener-Khintchine theorem [64] that

$$\langle |\tilde{\xi}|^2 \rangle = T_{msr} \,. \tag{2.14}$$

The expected value of the power spectrum density is given by a Lorentzian [50]:

$$\begin{aligned} \langle P_k \rangle &\equiv \langle |\tilde{x}_k^2| \rangle / T_{msr} \\ &= \frac{D}{2\pi^2 (f_c^2 + f_k^2)} \,, \end{aligned} \tag{2.15}$$

[5]The form for the Fourier transform of $\dot{x}$ is true under the limit $T_{msr} \to \infty$. See Appendix A.

with an exponential probability distribution of variance (Appendix A.4)

$$\mathrm{var}(P_k) = \langle P_k \rangle \,. \tag{2.16}$$

Here P_k is the power density at frequency f_k, f_c, the corner frequency (also called the particle's response, or roll-off frequency), is defined as

$$f_c \equiv \kappa/(2\pi\gamma_0)\,, \tag{2.17}$$

and D is the diffusion constant according to the Einstein relation

$$D = k_B T/\gamma_0 \,. \tag{2.18}$$

In principle, one can record a position series, take the power spectrum and fit it with Equation (2.15). The f_c extracted from the fit can then be used for determining κ according to Equation (2.17), given the bead radius R. In this method, errors in bead-size measurement and fluid viscosity will directly affect the trap-stiffness estimate. This problem is partly solved by the hybrid method ([49] and Section 2.4). Other useful treatments are applied to the raw data for ease of fitting (Section 2.3.4).

Note that the power spectrum method recovers the result of the equipartition theorem by integrating the power spectrum:

$$\langle x^2 \rangle = \sum_{k=-\infty}^{+\infty} \langle P_k \rangle \overset{T_{msr}\to\infty}{\longrightarrow} \frac{D}{2\pi f_c} \,. \tag{2.19}$$

Using the Einstein relation of Equation (2.18) and the definition of the corner frequency $f_c = \kappa/2\pi\gamma_0$, the result from the equipartition theorem Equation (2.6) is recovered. The power spectrum method of determining trap stiffness is superior to the equipartition method, since extraneous noise (low-frequency drift, discrete-frequency electrical and mechanical noise) is clearly distinguishable from the Lorentzian and can be treated accordingly. .

2.3.3 Hydrodynamical model of the trapped bead

The power spectrum is shown to be Lorentzian when assuming the viscous drag force is proportional to the bead velocity. However, this assumption is true only when the velocity field is stationary around the object. When the bead's motion relative to the surrounding

liquid is not a constant, the viscous force depends on the frequency of the specific motion mode and on the second derivative of the bead's position. This arises because the bead-fluid interaction generates propagating waves that then interact with the bead. The characteristic distance δ, or penetration depth, is the typical length that the wave propagates into the fluid. When the sphere is undergoing harmonic motion at low Reynolds number limit, the drag force exerted on the bead is [65]

$$F_{drag}(f) = -\gamma_0 \left(\left(1 + \frac{R}{\delta} \right) \dot{x} + \frac{1}{2\pi f} \left(\frac{R}{\delta} + \frac{2R^2}{9\delta^2} \right) \ddot{x} \right) , \tag{2.20}$$

where the penetration depth δ is related to the oscillation frequency f as

$$\delta = R(f_\nu / f)^{1/2} . \tag{2.21}$$

Here $f_\nu \equiv \nu/(\pi R^2)$, where ν is the kinematic viscosity. From the Fourier transform of Equation (2.20), the viscous force in the frequency domain can be expressed in terms of the Fourier transform of x:

$$\tilde{F}_{drag}(f_k) = -\gamma_0 \left(\left(1 + \frac{R}{\delta(f_k)} \right) (2\pi i f_k) + \frac{1}{2\pi f_k} \left(\frac{R}{\delta(f_k)} + \frac{2R^2}{9\delta(f_k)^2} \right) (2\pi i f_k)^2 \right) \tilde{x}_k . \tag{2.22}$$

Therefore the hydrodynamic drag coefficient can be defined as

$$\gamma(f_k) \equiv -\frac{\tilde{F}_{drag}}{2\pi i f_k \tilde{x}_k} \tag{2.23}$$

$$= \gamma_0 \left[\left(1 + \frac{R}{\delta(f_k)} \right) + i \left(\frac{R}{\delta(f_k)} + \frac{2R^2}{9\delta(f_k)^2} \right) \right] . \tag{2.24}$$

Because hydrodynamic effects occur at much higher frequency than the corner frequency (f_ν for a 2 μm-diameter bead in water is $\sim$ 300 kHz while $f_c \approx 1$ kHz), when including hydrodynamic effects in the theoretical analysis of the power spectrum, the inertial term in Equation (2.7) should be retained as the typical damping frequency is comparable to f_ν (see the definition of f_m below). With the inertial term and a complex γ, the power spectrum is calculated as

$$\langle P_k \rangle = \frac{D\mathrm{Re}(\gamma(f_k)/\gamma_0)}{2\pi^2 |f_c + i f_k \gamma(f_k)/\gamma_0 - f_k^2/f_m|^2} \tag{2.25}$$

$$= \frac{D\mathrm{Re}(\gamma(f_k)/\gamma_0)/(2\pi^2)}{[f_c + f\mathrm{Im}\gamma(f_k)/\gamma_0 - f_k^2/f_m]^2 + [f\mathrm{Re}\gamma(f_k)/\gamma_0]^2} . \tag{2.26}$$

Here, $f_m \equiv \gamma_0/(2\pi m)$ is a frequency related to the inertial relaxation time of the bead of mass m. Substituting $\gamma(f_k)$ from (2.24) into (2.26), the hydrodynamically corrected power spectrum is obtained:

$$\langle P_k^{hydro} \rangle = \frac{D[1 + (f_k/f_\nu)^{1/2}]/(2\pi^2)}{(f_c - f_k^{3/2}/f_\nu^{1/2} - f_k^2/f_{m^*})^2 + (f_k + f_k^{3/2}/f_\nu^{1/2})^2}, \tag{2.27}$$

where $f_{m^*} \equiv \gamma/(2\pi m^*)$ and $m^* \equiv m + 2\pi\rho R^3/3$. Because the density of polystyrene is close to water, f_m and f_{m^*} are related to f_ν: $f_{m^*} \approx 1.5 f_\nu$. In the actual fits, I use this simplification to eliminate f_{m^*}.

Further theoretical modifications to the power spectrum have been discussed in the literature [50]. When the bead is placed near an infinitely large plane as is the case in many optical tweezers instruments, the boundary will confine the the velocity field of the fluid, thereby increasing the effective drag force on the bead. Faxén derived the exact solution for the drag force on a bead at specific locations between two parallel walls [66]. For an arbitrary bead location, Oseen developed a reflection treatment that gives a good approximation to the actual drag force [67]. More recent theoretical [68] and experimental [69] studies have also attempted to address the effects of particle confinement. However, these treatments only deal with the drag force when the bead has a constant velocity, which is not the case for Brownian motion. K. Berg-Sørensen and H. Flyvbjerg combined the approximation of harmonic oscillatory bead motion with boundary effects, and calculated the drag coefficient in this situation [50]. This treatment gives the corrected drag coefficient in (2.26) as

$$\mathrm{Re}\,(\gamma(R/l)/\gamma_0) = 1 + \sqrt{\frac{f}{f_\nu}} - \frac{3R}{16l} + \frac{3R}{4l} \exp\left(-\frac{2l}{R}\sqrt{\frac{f}{f_\nu}}\right) \cos\left(\frac{2l}{R}\sqrt{\frac{f}{f_\nu}}\right) \tag{2.28}$$

and

$$\mathrm{Im}\,(\gamma(R/l)/\gamma_0) = -\sqrt{\frac{f}{f_\nu}} + \frac{3R}{4l} \exp\left(-\frac{2l}{R}\sqrt{\frac{f}{f_\nu}}\right) \sin\left(\frac{2l}{R}\sqrt{\frac{f}{f_\nu}}\right). \tag{2.29}$$

Here, l is the distance from the bead centre to the boundary, which can be as small as a few bead radii. For example in some optical tweezers setups, a molecule is stretched between a cover glass and trapped bead, and in magnetic tweezers instruments, the Brownian motion of the bead tethered to the chamber wall is likely to be affected by the nearby surface.

Moreover, a distinctive feature of the boundary effect is that unlike the vortices in fluid that decay exponentially with penetration depth δ, the effect of the boundary at larger separations is dominated by the $\sim 1/r$ decay in velocity of the flow. This long-range feature suggests that, even in our case where the bead is trapped roughly at the centre of a 160 μm-thick chamber, $l/R \sim 50$, the boundary effect is still of the order 2%.

In spite of the likely importance of the boundary effect to precise fits of the high-frequency part of the power spectrum, I did not include it in my analysis. The derivation of the hydrodynamic model with boundary effect (Equation (34) in [50]) drops the higher-order terms of parameter $\sqrt{f/f_\nu}$. In fact, this term is ~ 1 when fitting to high frequencies for bigger beads (f_ν for a 3.1 μm-diameter bead is $\sim$100 kHz) and should not be dropped. A correct determination of the effects of hydrodynamics and boundaries is beyond the scope of this thesis, and for simplicity, I include hydrodynamic effects but assume the boundary to be infinitely far from the bead. The systematic error introduced by this simplification is still less than the uncertainty of the bead-size determination (see below). Nonetheless, for a more reliable trap stiffness estimate, further investigation of the boundary effect will be necessary.

2.3.4 Data acquisition and compression

In the experiment, the position signal of the trapped bead is collected by the position-sensitive photodetector and its pre-amplifier, low-pass filtered, digitized by an A/D converter and sent to the computer, where the position signal is Fourier transformed to calculate the power spectrum. In the specific setup, the corner frequency of a trapped bead can range from 500 Hz to 3 kHz depending on bead size, laser power and optical alignment. In order to properly characterize the corner frequency, the Nyquist frequency f_{Nyq}, which is half of the sampling rate f_s, must be higher than the corner frequency. Even higher frequencies are required to see the effects of hydrodynamics discussed in the previous section. The maximum cumulative sampling rate of the A/D converter I used is 333 kSamples/s for all channels, meaning that f_s reaches 333 kHz only for a single channel measurement. In practise, I have chosen 300 kHz as the maximum sampling rate for one channel.

The frequency resolution is given by the reciprocal of the sampling length. At very low frequencies ($\sim$ 1 Hz and lower), contributions from external noise exceed the Brownian

motion of the bead (Appendix C.3). The sources of the very low frequency noise may include the thermal instability of the laser head, air density disturbance and the drift of optical elements.

Even though the very low frequency components are not useful for the fitting due to drift, it is still helpful to acquire long samples for smaller statistical dispersions. For long sampling time (100 seconds in this case), applying the power spectrum analysis to the entire data set is not efficient, therefore two data compression procedures, namely windowing and blocking, are introduced [50]. For each power spectrum of a series of position measurements, the power component at each frequency is exponentially distributed with a standard deviation of P_f. If I take a number of identical measurements and average all the spectra, the sample average will approach a Gaussian distribution about its expected value according to the central limit theorem. For a very long time series of position measurements, instead of directly taking the power spectrum, I slice it into small segments, each of which is long enough to obtain a frequency resolution sufficient to describe the Lorentzian shape of the power spectrum, take the power spectrum of each, and average these individual power spectra. This treatment is known as windowing (with a rectangular window function). If n_w is the number of windows, then the deviation of the windowed spectrum is narrowed to $\langle P_k \rangle / \sqrt{n_w}$. In signal analysis, various window functions can be applied to the raw signal to reduce leakage, but can result in signal distortion. In this treatment, since no peak-shaped feature is expected in the power spectrum, a rectangular window function suffices.

In addition to windowing, another data compression method called *blocking* is widely used. Since the Brownian motion gives a smooth Lorentzian form of the spectrum, in a small frequency range, the averaged values of frequency and the corresponding power density values can be taken to represent the data in this interval. For a block with width n_b discrete frequencies, the blocked frequency and power are

$$f^{block} = \frac{1}{n_b} \sum_{f_k \in block} f_k \,, \tag{2.30}$$

and

$$P^{block} = \frac{1}{n_b} \sum_{f_k \in block} P_k^{ex} \,. \tag{2.31}$$

When the blocked data are used in the fit, compared with the raw data, the error introduced by this treatment depends on the relative change of the fit value, the curvature of the fit

function and higher order terms. Specifically, it is shown that for an unwindowed power spectrum with exponential distribution, the relative deviation of the parameter probability estimate for the blocked data from the raw data is [50]

$$\Delta \log(p)_{block} - \Delta \log(p) = -\frac{1}{24}\left(\frac{n_b \Delta f P'(f^{block})}{P(f^{block})}\right)^2 + \mathcal{O}(P''\Delta f^2) + \mathcal{O}(\Delta f^3)\,. \quad (2.32)$$

Thus, as long as the leading higher order term $-\frac{1}{24}\left(\frac{n_b \Delta f P'(\bar{f})}{P(\bar{f})}\right)^2$ is much less than 1, blocking gives a reliable compression of the original data. In my data analysis procedure, the raw data is windowed before blocking, and therefore its distribution is approximated by a Gaussian instead. However, the deviation remains of the same order with a different coefficient. In the blocking procedure used here, the form in (2.32) is used.

To choose the proper block width, the simplest way is to estimate the largest value of $P'(f)/P(f)$, calculate the value of $n_b\Delta f$ necessary to keep the higher-order term less than one, and fix this blocking length globally over the whole frequency range. Actually for a fixed tolerance ϵ, the proper block width can be determined if an estimate of the corner frequency is known. Set

$$\epsilon = f_b \frac{P'(f)}{P(f)} \quad (2.33)$$

$$= f_b \frac{2f}{f_c^2 + f^2}\,, \quad (2.34)$$

where $f_b \equiv n_b\Delta f$. f is the central frequency of the block, and I have used the simple form (2.15) to describe the power spectrum. Assuming the start frequency of the block is given as f_0, then the length of this block f_b can be solved from

$$\epsilon = f_b \frac{2(f_0 + f_b/2)}{f_c^2 + (f_0 + f_b/2)^2}\,. \quad (2.35)$$

Following the dynamical scheme, one can determine the length of each block consecutively in a more adaptive fashion compared with the constant block width scheme. I followed this latter approach when blocking the power spectrum data.

2.3.5 Aliasing

If a continuous signal is recorded in discrete samples at a finite sampling rate, a frequency component at $f > f_{Nyq}$ will contribute its magnitude to a frequency between 0 and the

Nyquist frequency. This artifact due to a finite sampling rate is well known as aliasing. If the sampling rate is f_s, and therefore the Nyquist frequency $f_{Nyq} = f_s/2$, all frequency components outside the range $[-f_{Nyq}, f_{Nyq})$ will "fold" into this range:

$$\tilde{x}_k^{aliased} = \sum_{n=-\infty}^{\infty} \tilde{x}_{k+nN} \,, \tag{2.36}$$

where N is the number of samples, so $f_N = f_s$. Since $\tilde{x}_k$ are uncorrelated variables,

$$P_k^{aliased} \equiv \langle |\tilde{x}_k^{aliased}|^2 \rangle / T_{msr} \tag{2.37}$$

$$= \sum_{n=-\infty}^{\infty} P_{k+nN} \,. \tag{2.38}$$

It is discussed thoroughly in [50] that improper treatment of aliasing will cause significant systematic error. To avoid this in our experiments, a low-pass filter, acting as an anti-aliasing filter, is used right before data sampling. This removes high-frequency components but leaves the low frequency-components undistorted. The choice of filter depends on the specific application, but usually it is required to have minimum pass-band ripple, a narrow transition band, and sometimes a certain phase response in the pass band. In our case, I use a commercial 8-order Butterworth low-pass filter (LTC1064-2CN) and a second-stage second-order low-pass filter (f_{3dB} = 94 kHz, TL072CN, Texas Instruments) to prevent clock feed-through from the first filter.

The roll-off frequency of LTC1064-2CN is adjustable, which allows me to tune the optimal cutoff. Several factors must be taken into account. The pass band must cover the entire frequency range of interest with minimum distortion. Therefore the cutoff frequency f_{3dB} must be higher than the upper boundary of the power spectrum fitting range. The Nyquist frequency f_{Nyq} is a common choice for f_{3dB}; however, since the transition band is not infinitely narrow, frequency components beyond f_{Nyq} are not completely attenuated and therefore can still fold into the $[0, f_{Nyq})$ range, thus distorting the spectrum. In order to have the largest undistorted pass band, it is proper to place the Nyquist frequency in the middle of the transition band of the filter. Given the maximum practical Nyquist frequency of 150 kHz (for a single channel, bandwidth limited by the A/D converter), I set f_{3dB} at 60 kHz and use a fitting range from 0 to 30 kHz in the analysis of the power spectrum. Therefore the closest frequency to be aliased to this fitting range is 270 kHz or $4.5 f_{3dB}$,

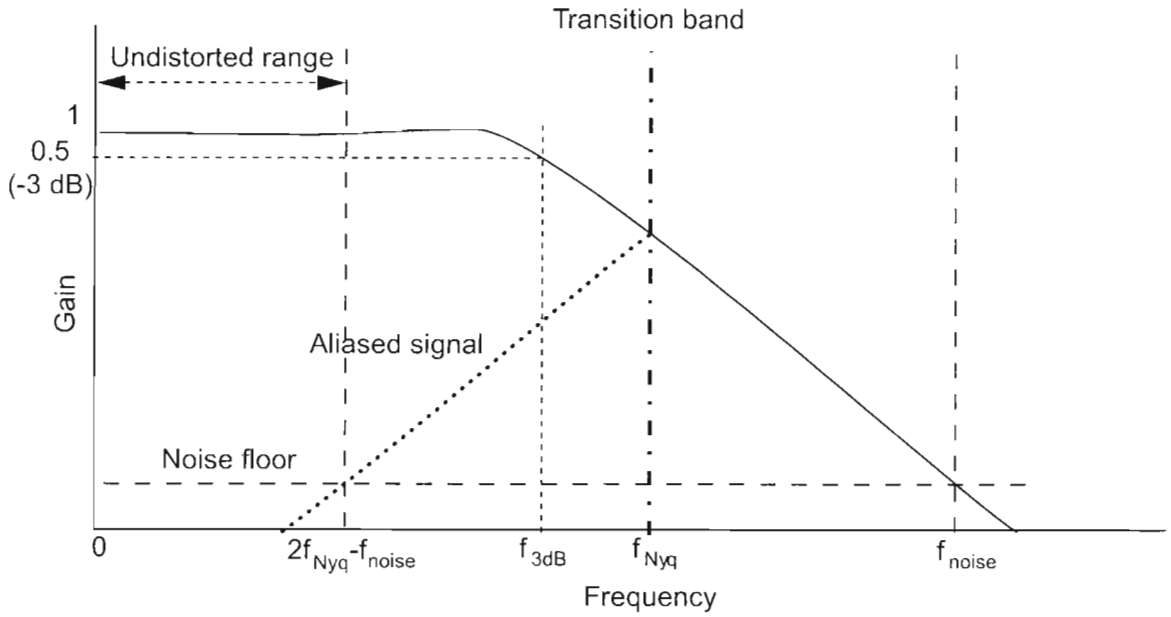

Figure 2.5: Anti-aliasing schematic, with a linear frequency axis and logarithmic gain axis. The solid line shows the frequency response of the low-pass filter. All signal above the Nyquist frequency f_{Nyq} will be reflected to the band below f_{Nyq}, with attenuation by the filter (reflected dotted line). Above a certain frequency f_{noise}, high-frequency components are attenuated below the noise floor of the A/D converter. Thus at frequencies below the aliased frequency ($2f_{Nyq} - f_{noise}$), the experimental spectrum is undistorted. In our experimental implementation of this scheme I chose the cutoff frequency of the filter (f_{3dB}) such that it is lower than the Nyquist frequency f_{Nyq}.

where the attenuation of the anti-aliasing filter is over 80 dB, much lower than the noise floor of the A/D converter (Figure 2.5).

Because of the design of the filter, when f_{3dB} is set larger than 30 kHz, an overshoot in the transition band occurs, roughly peaked at 50 kHz (Figure B.1). This is relevant since for typical values of window number and block width $n_w = 100$ and $n_b = 100$, the relative variance of the power spectrum is $1/\sqrt{n_w n_b} = 1\%$, whereas the distortion of the filter exceeds this value above 20 kHz. In order to obtain proper information about the hydrodynamic behavior of the bead, a bandwidth up to 30 kHz for fitting the power spectrum is necessary, meaning that the proper knowledge of the filter's response is required. I mea-

sured its response and include this experimental correction in all estimates of the power spectrum used in the following fittings (Appendix B).

Because aliasing is a well understood process, in principle it is possible to calculate its effect and compensate for it. To do that, the frequency response of the detector and amplifier up to frequencies for which the gain is below the noise floor of the electronics must be known. The A/D converter behaves as a low-pass filter with cut-off frequency 470 kHz as specified by the manufacturer and verified by my measurements. The photodetector also has a low-pass effect since its silicon substrate has a poor absorption of long wavelength IR photons[6]. However for the 835 nm light used here, the cut-off frequency of our PSD is at least higher than the A/D converter. The main problem in determining the frequency response of the detection system comes from the PSD pre-amplifier. The amplifier works in a current-amplifying mode, which has a strong coupling between load and the amplifier. The frequency response thus depends strongly on the load, making it hard to measure using a variable dummy load. Nevertheless, I determined its cut-off frequency to be in the range of 200 kHz to 400 kHz. This is thus the limiting factor for the high-frequency response of the system, and because of its load dependence, this effective cutoff frequency is unknown. Because of this uncertainty, it is not possible to correct the power spectrum by accounting for the aliasing in the measurement, and so the low-pass filtering approach described in the previous paragraphs is employed.

2.3.6 Results

I calibrated the trap using the routines described above. The position signal from the PSD is first low-pass filtered with a cut-off frequency set at $f_{3dB} = 60$ kHz for anti-aliasing. The filtered signal is sampled at 300 kHz for 100 s for horizontal and vertical channels separately.

First, the variance of each slice is calculated from the position signal and is used to determine the trap stiffness using the equipartition theorem. For a 3.1 μm-diameter trapped bead, the variances of horizontal and vertical directions are calculated as 2.52×10^{-5} V^2

[6]It is reported that for a 1064 nm wavelength IR laser detected by a quadrant photodiode (QPD), the cut-off frequency can be as low as 10 kHz [70]. However in our case where a lateral-effect PSD is in use instead of a QPD, the effect of IR transparency on the thin silicon substrate is to lower the sensitivity of detection rather than to reduce the frequency response.

Table 2.1: Fitting parameters for a simple Lorentzian power spectrum fit for a 3.1 μm-diameter trapped bead.

channel	x	y
corner frequency f_c (Hz)	454 ± 1	429 ± 5
diffusion constant D (V^2/s)	0.07086 ± 0.00008	0.08255 ± 0.0009
trap stiffness κ (pN/μm)	83 ± 3	78 ± 3
χ^2	5350	5501
number of points to fit	101	101

and 3.10×10^{-5} V^2 respectively, or $2.77 \times 10^{-5} \mu m^2$ and $2.26 \times 10^{-5} \mu$ m^2, converted using the result in 2.2.4. The local temperature of the bead is set to be equal to the room temperature of 295 K, a treatment that ignores the (minimal) local heating effect of the laser. From Equation (2.6), the trap stiffness is then quickly calculated as $\kappa_x = 147$ pN/μm and $\kappa_y = 180$ pN/μm.

For determination of the trap stiffness using the power spectrum method, the position signal is sliced to 100 windows, then the 100 sets of windowed data are Fourier transformed to frequency space. The power density is determined for each, and the average of the 100 power spectra is taken. Finally the averaged spectrum is blocked as described in Section 2.3.4 with dynamic block widths. The blocked power spectrum is then fit first with the simple Lorentzian of Equation (2.15) with results indicated in Figure 2.6 and Table 2.1. To calculate the trap stiffness, I used the 3.1 ± 0.1 μm nominal value as the bead diameter.

From the χ^2 value and the residual, it is clear that even though the power spectrum has a overall low-pass shape, a simple Lorentzian does not describe the behavior of the trapped bead properly. The cause of the discrepancy is not the response of the low-pass filter that is ignored in the fit, because the response is flat below 10 kHz (Appendix B). Therefore for a reliable estimate of the parameters, further corrections to this simple model must be considered. I observed that for the smaller 1.2 μm-diameter bead for which the hydrodynamic effect is less significant, χ^2 is about 6 times larger than the number of points. If the sample time is 10 times shorter, the systematic discrepancy will be covered by the Brownian randomness, *i.e.*, the residuals become insignificant and the true value falls within the larger error bar. When precision is not a concern, short sample lengths ($\sim$ 10 s) and fits to the simple Lorentzian (2.15) can return usable estimates of the corner frequency for

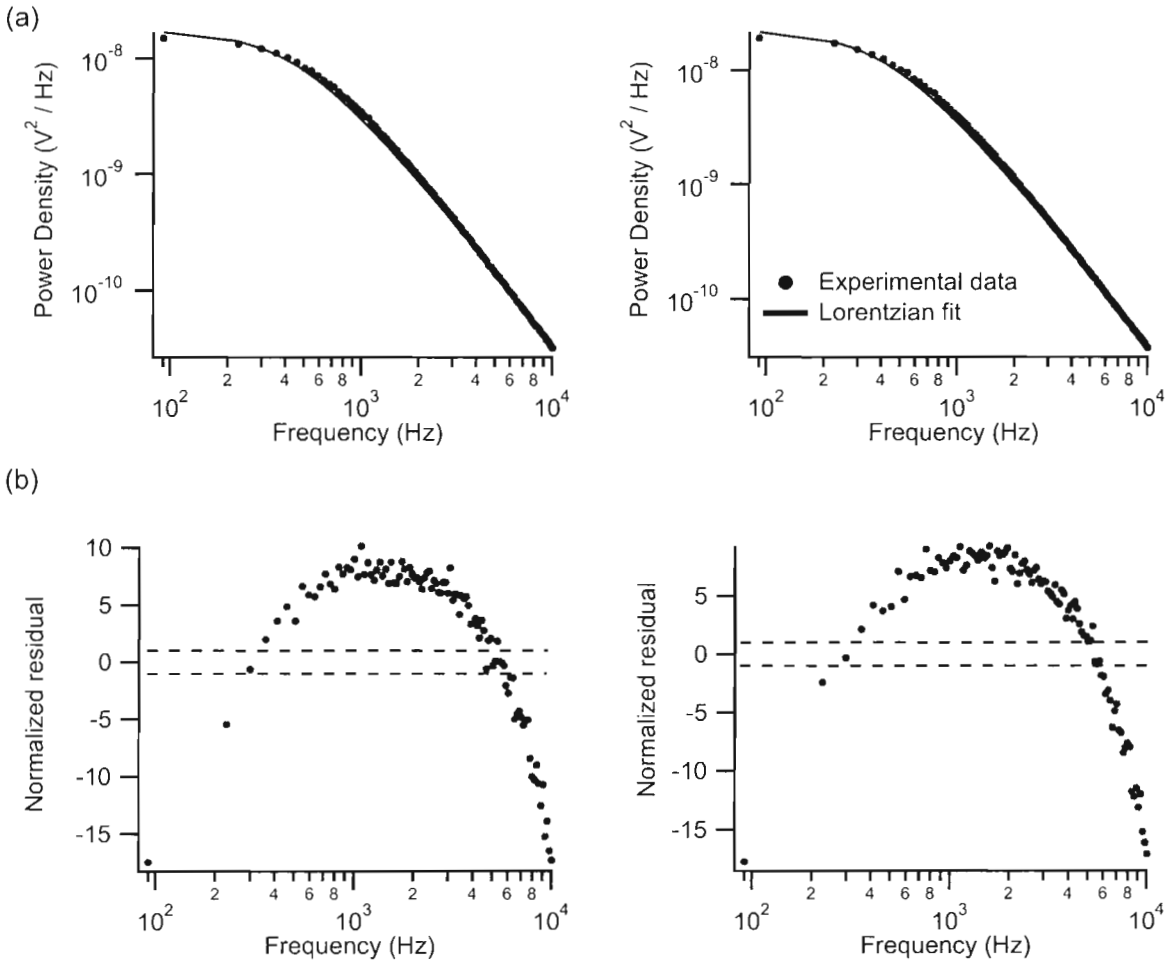

Figure 2.6: The blocked power spectra and their fits with a simple Lorentzian for a 3.1 μm-diameter polystyrene bead from 1 Hz to 10 kHz in horizontal (x) and vertical (y) directions. (a) The power spectrum and its fit. The raw data are windowed and blocked as described in the text and are fit with Equation (2.15), without correction for the anti-aliasing filter. The fitting parameters are listed in Table 2.1 (b) The normalized residual plot of the fit. The deviation is normalized by the expected deviation $\langle P_k \rangle$ and the number of averages $\sqrt{n_b n_w}$. The two dashed lines indicate the distance of the expected standard deviation. χ^2 for the fit are 5350 for horizontal direction and 5501 for vertical direction compared with 101 points being fit.

small bead size.

To obtain a more precise estimate of the fitting parameters, the power spectra are fit with the complete model in Equation (2.27), which includes hydrodynamic effects, as well as including compensation for the anti-aliasing filter (Figure 2.7and Table 2.2). In fitting the power spectra, the diffusion constant D, corner frequency f_c and f_ν are set to be fitting parameters. The uncertainties are estimated from the covariance matrix, and χ^2 is calculated from the deviation of the experimental power spectrum from the expected values. Since f_ν is directly related to the bead size ($f_\nu = \nu/(\pi R^2), \nu = 1\mu m^2/\mu s$ for water), the bead diameter is shown in Table 2.2 for comparison as well. I apply the same process for 1.2 μm-, 2.1 μm- and 3.1 μm-diameter beads for both horizontal and vertical directions. The results are listed in Table 2.2. For comparison between the simple Lorentzian fit and full hydrodynamic model, the experimental data in Figures (2.6) are fit with the corrected model with results shown in Figure (2.7).

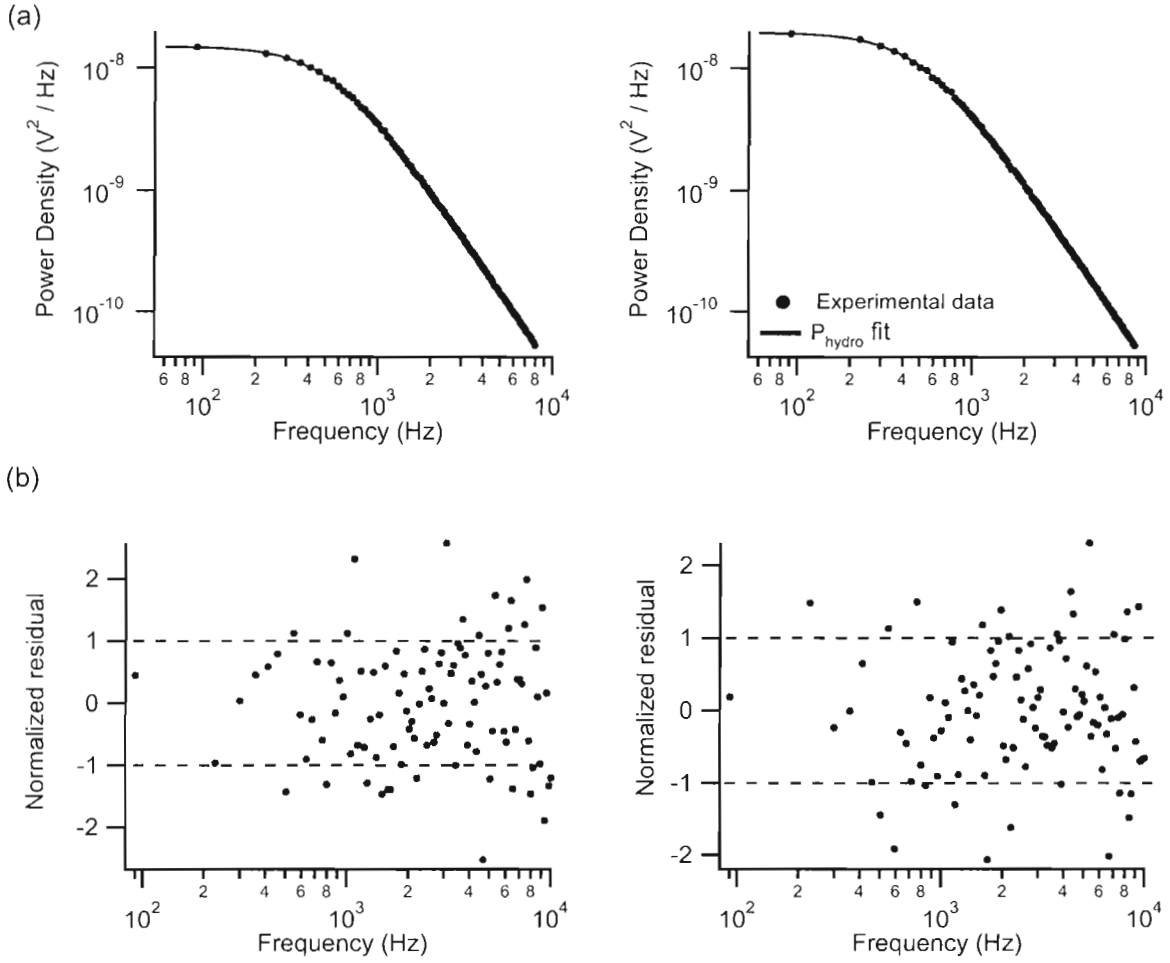

Figure 2.7: The blocked power spectra for a 3.1 μm-diameter polystyrene bead from 1 Hz to 10 kHz. The same data are shown in Figure (2.6), but here are fits with the hydrodynamically corrected model (2.27). The fit parameters are listed in Table 2.2. Here, the normalized residuals fall within the expected $\pm$ one standard deviation, as indicated by the dashed lines.

Table 2.2: Power spectrum fitting results of beads of 3 different diameters. The trap stiffness is calculated using the bead size value from the fit instead of the nominal value from the manufacturer.

	1.2 μm bead	
channel	x	y
fitting range (Hz)	$50 - 30000$	$50 - 30000$
corner frequency f_c (Hz)	3250 ± 4	3356 ± 4
diffusion constant D (V^2/s)	1.731 ± 0.002	2.435 ± 0.003
f_ν (kHz)	816 ± 20	885 ± 20
bead diameter d (μm)	1.25 ± 0.06	1.20 ± 0.06
trap stiffness κ (pN/μm)	240 ± 12	238 ± 12
PSD sensitivity (V/μm)	2.24	2.60
χ^2	143	142
number of points to fit	145	145

	2.1 μm bead	
channel	x	y
fitting range (Hz)	$1 - 20000$	$1 - 20000$
corner frequency f_c (Hz)954 ± 2	926 ± 2	
diffusion constant D (V^2/s)	0.2175 ± 0.0005	0.2867 ± 0.0006
f_ν (kHz)	280 ± 6	287 ± 6
bead diameter d (μm)	2.13 ± 0.09	2.11 ± 0.09
trap stiffness κ (pN/μm)	121 ± 5	115 ± 5
PSD sensitivity (V/μm)	1.04	1.18
χ^2	129	153
number of points to fit	129	129

	$3.1\mu m$ bead	
channel	x	y
fitting range (Hz)	$1 - 10000$	$1 - 10000$
corner frequency f_c (Hz)	541 ± 1	513 ± 1
diffusion constant D (V^2/s)	0.0885 ± 0.0003	0.1037 ± 0.0003
f_ν (kHz)	130 ± 4	126 ± 4
bead diameter d (μm)	3.14 ± 0.20	3.17 ± 0.20
trap stiffness κ (pN/μm)	100 ± 6	96 ± 6
PSD sensitivity (V/μm)	0.80	0.87
χ^2	91	73
number of points to fit	101	101

In the chosen fitting ranges, the hydrodynamic model agrees with experimental data for all three different sized beads, as shown by reasonable values of χ^2 ($\chi^2 \sim N_{points}$). Also from the residual plots, it is clear that the theory works well statistically (See Figure 2.7 for the residual for the 3.1 μm-bead, same data as shown in Figure 2.6). For a 100-second-long sample, the important fitting parameter for trap stiffness determination, f_c, has an error bar of about 0.2%, as does the apparent diffusion constant D. In comparison with the simple Lorentzian fitting, the hydrodynamic model gives a 20% higher, and much more precise estimate of the corner frequency. The third fitting parameter f_ν, or indirectly the bead diameter, has a larger uncertainty. This is because hydrodynamical effects, which are characterized by f_ν, become apparent only at the high frequency range, and the upper ranges of fitting barely reach the frequency where the spectra start to be sensitive to the bead size. Nonetheless, the power spectrum fittings still give a very accurate estimate of the bead sizes.

The sizes of the beads are small enough that optical artifacts from imaging with the microscope objective makes it hard to evaluate the bead size using video microscopy. The image of the bead usually has a dark ring around the bead, and the width of the ring depends specifically on the focal depth of the bead and the illumination conditions. The accurate size of a specific bead also cannot be obtained from the nominal size for the batch of the beads since individual beads can have significant deviation from this value, usually $\pm 0.1\mu$m. The hydrodynamical model gives comparable estimate of the bead size, simply by fitting the

power spectrum to Equation (2.27).

Another test of the fit is the calibration of the photodetector signal calculated from the apparent diffusion constant of the refracted laser signal. When the bead size is known, the diffusion constant can be calculated from the Einstein relation

$$D = k_B T/\gamma_0 = \frac{k_B T}{6\pi\rho\nu R},$$

where R is the bead radius. By comparing D calculated with this relation from the bead size obtained from the power spectrum fit with the apparent diffusion constant from the fit in unit of V^2/s, the scaling factor ($V/\mu m$) can be calculated. The scaling factors for different bead sizes are listed in Table 2.2. For the 3.1 μm-bead, the result falls in a reasonable range but does not agree within the error of the calibration using the piezoelectric stage, given in Section 2.2.4. The difference could result from the use of two different beads in the two measurements and the realignment of optics in our instrument.

Although D and f_c are determined with good precision, neither is a direct measure of the trap stiffness. The apparent diffusion constant (V^2/s) is related to the absolute diffusion constant ($\mu m^2/s$), but the scaling factor ($V/\mu m$) of the position detection is required. The calibration is problematic because the magnification depends on the bead size. The trap stiffness determination from the corner frequency requires the drag coefficient, which is a function of the bead size and the viscosity of the surrounding media. In Table 2.2, the trap stiffness is calculated from the bead diameter determined by the fit to the spectrum, and therefore has a relatively large error bar.

The correlation between fitting parameters is calculated from their covariance matrix. I found that the deviation of the estimated D and f_c has a correlation of 0.55, suggesting a valley-shaped parameter likelihood distribution. However, since the uncertainty is already compressed below 0.2% by the long sample length, these two parameters are well determined by this method.

Because motion at frequencies much higher than the corner frequency approaches free Brownian motion, it does not contain much information about the optical trap. Therefore, pushing the upper boundary of the fitting range much beyond the corner frequency does not narrow the error bars of the corner frequency and the diffusion constant (Table 2.3). However, the bead-size-related hydrodynamic effects have a characteristic frequency f_ν at $\sim$ 100 kHz for a 3.1 μm-bead and $\sim$ MHz range for a 1.2 μm-bead, and thus increasing the

Table 2.3: Effect of the upper fitting boundary on fitting parameters from the power spectrum. (2.1 μm bead, channel x. The lower fitting boundary is set at 10 Hz in all cases.)

upper boundary (kHz)	f_c (Hz)	D (V^2/s)	d (μm)
1	942.4 ± 8.8	0.213 ± 0.006	2.5 ± 2.9
2	947.2 ± 3.9	0.2169 ± 0.001	1.9 ± 1.1
3	948.1 ± 3.0	0.2167 ± 0.0008	2.04 ± 0.70
5	948.6 ± 2.4	0.2168 ± 0.0008	2.05 ± 0.39
10	951.1 ± 2.0	0.2073 ± 0.0006	2.13 ± 0.19
20	949.1 ± 1.9	0.2168 ± 0.0005	2.09 ± 0.10

upper boundary reduces the uncertainty of the bead size (Table 2.3).

Since the frequency response of all electronics including the anti-aliasing filter is characterized up to 50 kHz, the power spectrum measurement is accurate up to this frequency. However, in the actual fitting I find that the experimental power spectra have a significant deviation from the theoretical prediction above a certain frequency depending on bead size. The cause of this systematic deviation is unclear. One possible cause could be the systematic error introduced by ignoring boundary effects and/or ignoring nonlinear terms when treating the hydrodynamics of the bead .

The three treatments, the equipartition theorem method, the simple Lorentzian fit and the hydrodynamic model, give different values of the trap stiffness. The equipartition theorem method does not distinguish the variance of the bead arising from thermal motion from noise from other sources. In addition, the position variance estimate in real units depends on the sensitivity of the PSD. This procedure can introduce severe systematic error into the trap calibration because the sensitivity depends on the alignment, bead size, and the specific location of the bead in the focal area, and therefore the pipette-tip calibration can deviate from the actual trapping condition significantly. The discrepancy between trap calibration by the equipartition method and the power spectrum method can be shown to arise in part from the different values of the PSD sensitivity. The simple Lorentzian power spectrum method, as discussed earlier, is limited by its over-simplified model. Here too one must use predetermined bead size or the conversion factor for the PSD sensitivity. Thus this method should only be used for a quick determination of the trap stiffness (<10 s), when precision is not a requirement. The hydrodynamic model works well for the real data (up to $\sim$ 30 kHz

in our instrument), and should be used for quantitative applications of the optical tweezers.

2.3.7 Cross-talk between channels

It is stated in [50] that in their experiments, cross-talk between x and y channels was $\sim 5\%$. The reasons for this, as Flyvbjerg *et al.* suggested, could be ellipticity of the trapping potential and/or the nonlinear relation between beam displacement and voltage output from the quadrant photodiode (QPD) they used. I tested the correlation of the two channels to see if this is an issue for us. The sampling rate was set to be 150 kHz for this two-channel measurement.

According to the cross-correlation theorem, the correlation of two signals can be expressed in terms of the product of their Fourier transforms. I plot $P_{xy}/(P_x P_y)^{1/2}$ as an indication of correlation, where P_{xy} is defined as

$$P_{xy} = \tilde{x}\tilde{y}^* \,, \tag{2.39}$$

where the asterisk represents the complex conjugate.

Similarly to [50], I observe a -2% correlation between horizontal and vertical channels (Figure 2.8). In our case, the photodetector I use is a lateral-effect photodetector instead of a QPD, therefore the position-voltage response is linear over a much larger range. The presence of the correlation in this experiments suggests therefore the possibility of ellipticity of the trapping potential. Because the microscope objective is over-filled by the trapping beam, if the trapping beam is not perfectly aligned with the axis of the objective, the beam will have different momentum in two orthogonal directions, resulting in an elliptical trap potential. This is a possible explanation for the correlation of the two channels. I also observed that the correlation depends on the orientation of the PSD, which confirms the hypothesis that the cause of this correlation is the shape of the trapping potential. Further test is suggested if the misalignment results in significant correlation.

2.4 Hybrid method to determine the diffusion constant

The power spectrum of a thermally driven bead gives precise information about the corner frequency and the diffusion constant. The frequency is correctly extracted because of

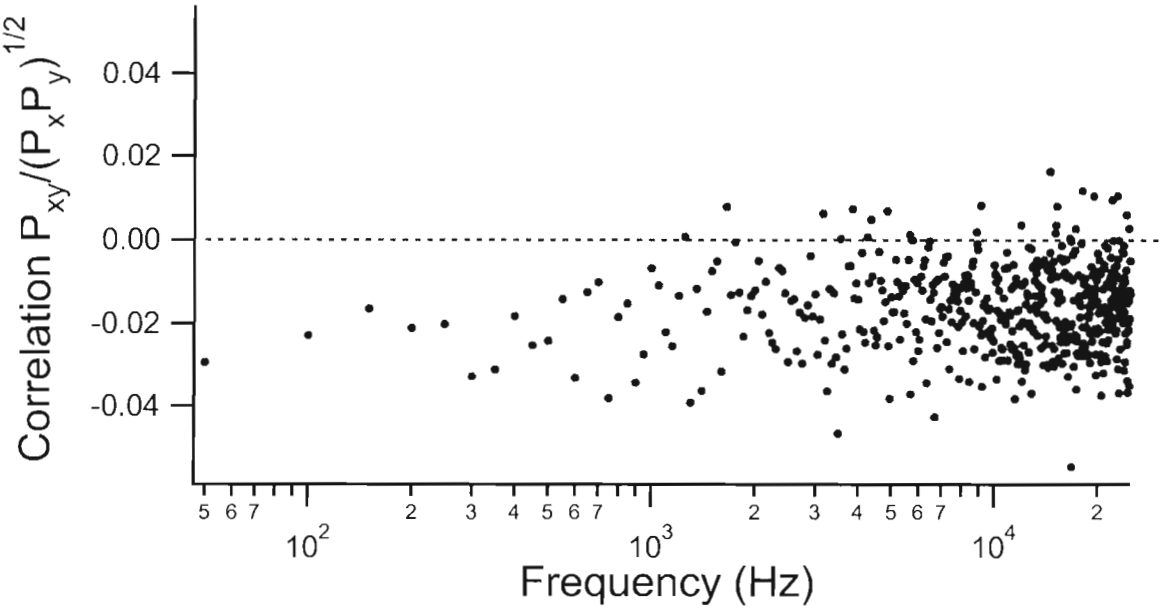

Figure 2.8: The correlation spectrum between horizontal and vertical channels, characterized by $P_{xy}/(P_x P_y)^{1/2}$. The data is for the same bead as in Figure 2.7, but sampled at 150 kHz for two channels simultaneously and windowed at 0.02 s instead of the 1 s applied in Figure 2.7. In this test, a -2% correlation is observed. The reason for this correlation could be an elliptical shape of the trap and its mismatch with the measurement axis of the PSD.

the precise clock time of the A/D converter; however, the diffusion constant is measured in units of the position sensor signal, with a unknown conversion factor to real bead displacement. To recover the trap stiffness in real displacement units, I use the bead size from either the high-frequency hydrodynamics or the nominal value from the manufacturer in the calculation. In the trap stiffness calculation, the uncertainty in bead size is the dominant contribution to the uncertainty in trap stiffness, since the corner frequency is determined with very high precision.

This problem can be solved if extra information is introduced. When the bead is driven by a known external force, the response can be measured and compared with the predictions from the magnitude of the driving force, allowing the position sensor to be calibrated. Tolić-Nørrelykke *et al.* combined the power spectrum method with a sinusoidal driving force, obtaining high precision in the determination of a bead's diffusion constant [49]. Since our instrument is capable of performing this experiment and a small error in trap stiffness is our goal, I repeated their experiment on our instrument.

In the experiment, the piezoelectric stage is driven sinusoidally while the position of the bead is recorded. In addition to the thermal force, the bead is also driven by the motion of the surrounding fluid. Assume that the position of the stage is

$$x_{drive}(t) = A\sin(2\pi f_{drive}t)\,. \tag{2.40}$$

A trapped bead in this moving media will experience a drag force

$$F_{drag} = \gamma_0(\dot{x}(t) - \dot{x}_{drive}(t))\,, \tag{2.41}$$

Here $\dot{x}(t) - \dot{x}_{drive}(t)$ is the relative motion of the bead with respect to the fluid. Note that this expression ignores the hydrodynamical effect at high frequencies[7]. The equation of motion of the bead with this external driving force becomes

$$\gamma_0\dot{x} + \kappa x = \sqrt{2D}\xi(t) + \gamma_0\dot{x}_{drive}(t)\,. \tag{2.42}$$

[7]Under the linear simplification of hydrodynamics, the only factor that matters is the the ratio between the thermally driven motion power density characterized by D and the externally driven power density $A^2 f_{drive}^2\delta(f - f_{drive})$. All the hydrodynamical corrections do not change this ratio and therefore the PSD sensitivity calibration is unaffected, even though the absolute values of both will change. In any case, at the 15 Hz driving frequency used in these experiments, the counter-action is negligible.

The difference compared with the previous treatment of equation (2.11) is the driving term. Following the approach of Section 2.3.2 to solve this equation, the power spectrum density of a driven bead in a thermal environment is

$$P_{driven}(f) = \frac{D}{2\pi^2(f^2 + f_c^2)} + \frac{A^2 f_{drive}^2/4}{f_{drive}^2 + f_c^2}\delta(f - f_{drive}) . \tag{2.43}$$

The magnitude of the oscillation A at the driving frequency can be measured in real units. Additionally, the ratio between the amplitude of driven oscillations and the thermal motion is fully described in the power spectrum in Equation (2.43). Thus, from the measured power spectrum in undetermined scales and knowledge of A (in real units), the diffusion constant in real units is recovered. Note that the response of the motion to the external driving power $A^2 f_{drive}^2$ follows a Lorentzian as a function of driving frequency f_{drive}, as shown in the second term of the right hand side of Equation (2.43).

For a finite sample length, the power spectrum is evaluated at discrete frequencies. Because of this, a single frequency component may contribute signal to the evaluated power at nearby frequencies. This artifact of finite sample length is known as "leakage". In the evaluation of the power spectrum, it is particularly problematic for the power spike at f_{drive} because the total power of one frequency component is hard to evaluate if it is broadened into a wider frequency range. Window functions are used in signal processing to obtain a narrow power distribution, but this treatment causes some distortion of the signal. The way to solve this problem is to set the sample length as an integer multiple of the driving period. The power density of the driven oscillation is then confined to just one discrete frequency component (see Appendix A.3 for details). If the sample length is T_{msr}, and therefore the frequency resolution $\Delta f = 1/T_{msr}$, the spectrum of a harmonic oscillation with amplitude A and a frequency f_{drive} is an integer multiple of Δf. This specific choice of sample length results in a single peak with height $A^2 T_{msr}$ or $A^2/\Delta f$.

In this way, the problem of converting the PSD voltage measurement in order to recover the diffusion constant in real units is solved. The displacement of the surrounding fluid is controlled and measured in real units. The power at the driving frequency is calculated according to Equation 2.43, but the motion is measured by the PSD in units of volts. Letting β be the conversion factor from displacement to voltage, the theoretical height of the power

density as measured from the PSD at the driving frequency is

$$P_{drive}^{PSD}(A) = \frac{D^{PSD}}{2\pi^2(f_{drive}^2 + f_c^2)} + \frac{f_{drive}^2/(4\Delta f)}{f_{drive}^2 + f_c^2}\beta^2 A^2 \,, \tag{2.44}$$

>From the relation between the measured power at the driving frequency and the variable driving amplitude A, the conversion factor β can be determined. The actual diffusion constant $D(\mu m^2/s)$ is then determined by $D^{PSD}(V^2/s)$ and $\beta(V/\mu m)$:

$$D = D^{PSD}/\beta^2 \,. \tag{2.45}$$

Finally, with a reliable estimate of the diffusion constant, the absolute value of the trap stiffness can be determined. From the Einstein relation $k_BT = D\gamma_0$ and the definition of the the corner frequency $f_c = \kappa/2\pi\gamma_0$,

$$\kappa = \frac{f_c D}{2\pi k_B T} \,. \tag{2.46}$$

Because the temperature is well regulated in the laboratory to within ± 0.2 K, the thermal energy k_BT has a small contribution to the total error of κ. The absorption of light by the trapped bead is negligible since the power of the transmitted laser does not change significantly with and without a bead trapped.

As a cross-check of the results of the above calculation, the bead size is calculated from the diffusion constant determined by Equation (2.45):

$$R = \frac{\gamma_0}{6\pi\rho\nu} \tag{2.47}$$

$$= \frac{k_BT}{6\pi\rho\nu D} \,. \tag{2.48}$$

This result is compared to the nominal value of the bead size and to the result obtained from the high frequency hydrodynamics treatment.

The layout of the experimental setup remains mostly the same as used for the "stationary" power spectrum measurement. Here the driving signal is delivered from an analogue output on the National Instruments PCI-6052E card, and is fed to the analogue input of the driver of the piezoelectric stage. The actual motion is measured by the built-in position sensor on the piezoelectric stage, and is digitized by the A/D converter on the data acquisition card. Explicitly, the driving frequency is set at 15 Hz with 20 variable amplitudes

because this frequency is well below the bandwidth limit of the piezoelectric stage, but high enough to give a distinct peak in a typical power spectrum. At each amplitude, the position of the trapped bead read by PSD is recorded at 250 kHz for 5 seconds. After each position measurement, the sensor voltage of the stage is recorded at 2 kHz for 1 second to extract the driving amplitude. The stage position signal is not taken simultaneously with the PSD data due to bandwidth limitations of the A/D converter. The 20 time series are Fourier transformed for power spectra, each windowed at 1 Hz and blocked in the same way described in Section 2.3.4. Figure 2.9 shows a a representative power spectrum of a driven bead. For regular power spectrum fitting of thermal motion, the 20 blocked spectra are averaged for maximum usage of data and the point at 15 Hz is omitted. This is valid because the driving force does not have contributions at frequencies other than the driving frequency under the assumption that the system is linear. The power spectrum is then fit with the hydrodynamical model (Equation 2.27) from 40 Hz to 20 kHz to extract f_c and D^{PSD}. To determine the actual driving amplitudes, the 20 sets of stage sensor signal are fit with sinusoidal functions. Finally the 20 peak power density values at 15 Hz are plotted against the square of the driving amplitudes and fit with a straight line (Figure 2.10). The PSD conversion factor β, the diffusion constant D in real units and the trap stiffness κ are then calculated.

In principle, with the aid of an external driving force, the bead radius is well characterized. It is an independent measurement of the high-frequency hydrodynamical effects discussed in the previous sections, and therefore can serve as an examination of the accuracy of these methods. The peak height-A^2 curve shows a good linear relation (Figure 2.10), redsuggesting that the shape of the optical trap is harmonic up to the magnitude of the harmonic-driven motion ($\approx$10 nm); the magnitude of the thermal background falls into the error range of the intercept of the fit. Typical relative error of the slope is around 1% or better, indicating a high precision estimate. However, in preliminary experiments on different beads, the bead size derived from the PSD sensitivity β and the diffusion constant in V show a systematic trend that the bead size derived from horizontal measurements is roughly 5% larger than that from the vertical scans (*e.g.* $R_x = 3.15 \pm 0.05\mu$m and $R_y = 2.93 \pm 0.06\mu$m for a 3.1 μm-diameter bead), whereas in the actual case of a spherical bead, these values should be identical. In comparison, the high-frequency hydrodynamical results yield better agreement between x and y but with larger uncertainties. The reason for this discrepancy

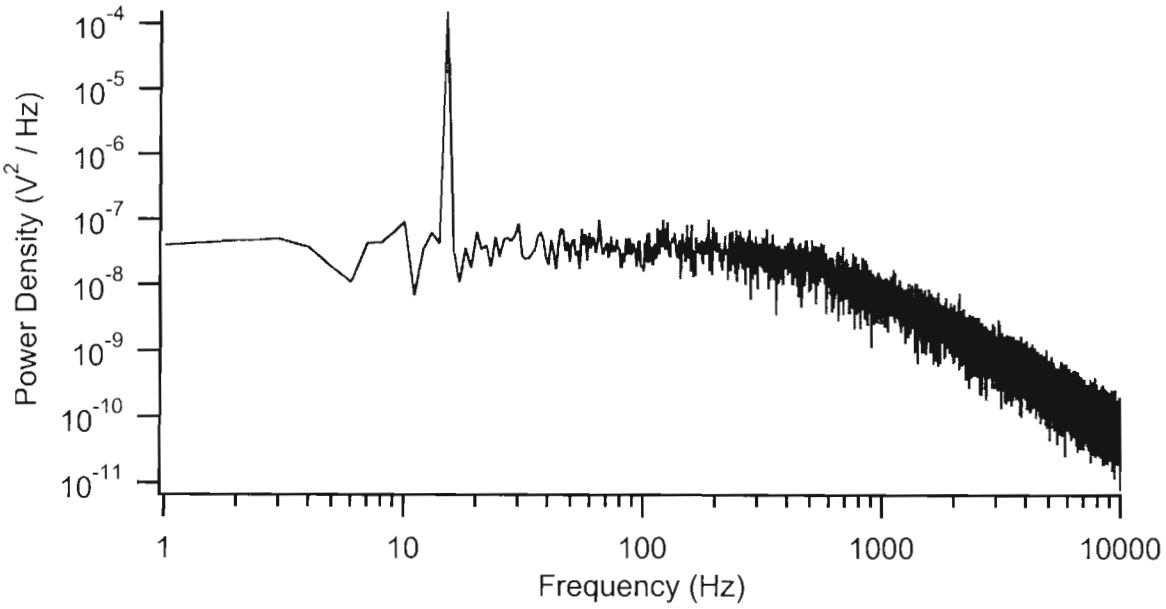

Figure 2.9: A power spectrum of an externally driven bead (1.2 μm diameter). Data was sampled for 5 seconds and sliced in 5 windows. 20 measurements were taken in series with different driving magnitudes. In addition to the normal thermal noise spectrum, a single spike at the drive frequency (15Hz) indicates how the bead responds to the external perturbation. The sample length (5 s) was chosen such that the harmonic driving force has only one frequency component in the spectrum as shown.

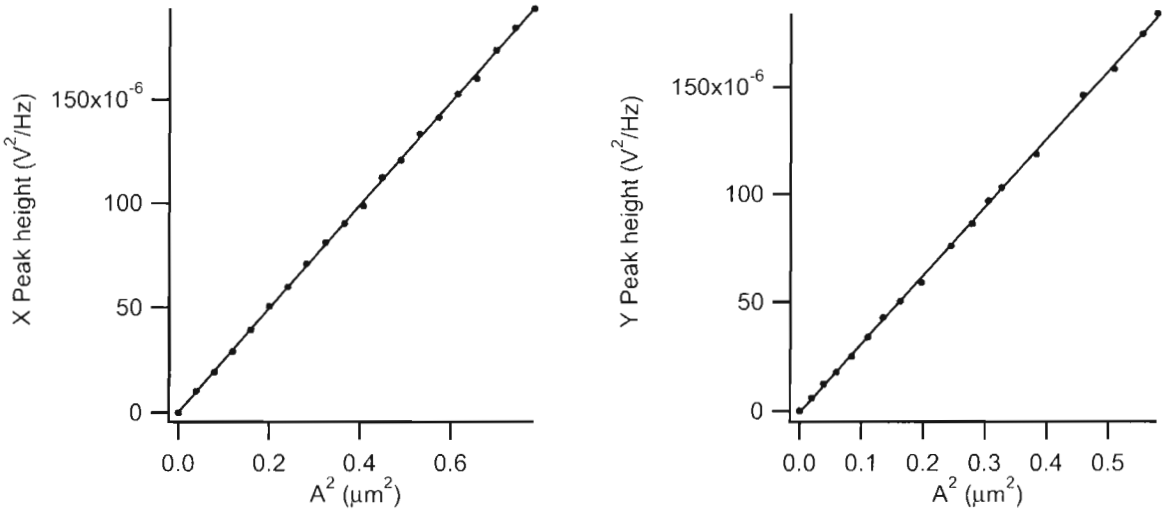

Figure 2.10: The height of the peak at the driven frequency plotted against A^2 for a 3.1 μm-bead in horizontal (x) and vertical (y) directions. The driving magnitudes were set at 20 different values and the height of the spikes was obtained from the power spectra at the driving frequency 15 Hz. The good linear relation in the plots indicates the ability to estimate the diffusion constant in real units in high precision.

is not clear yet. Multiple factors can contribute to the disagreement, most possibly the asymmetry of the trap potential due to optical misalignment. Further tests must be carried out.

2.5 Shape of the trapping potential

The analysis presented in this thesis is based on a harmonic potential with a linear force-displacement relation. Experimentally this assumption is only true over a finite range. The anharmonicity of the trapping potential will have effects on the shape of the power spectrum, but also quickly complicates the equation of motion. The nonlinear Langevin equation has been treated in the literature [71], but the discussion of its application in optical tweezers is not present.

Since the behaviour of the system is time-independent (apart from the stochastic, thermally driven motion of the bead), the ensemble distribution of bead positions can be described by Boltzmann's theorem. In thermal equilibrium, the potential $U(\mathbf{x})$ is then related to the probability density $p(\mathbf{x})$ of finding the bead at certain location:

$$p(\mathbf{x}) \propto \exp(\frac{-U(\mathbf{x})}{k_B T}) \,. \tag{2.49}$$

Experimentally, one can plot a two-dimensional histogram of bead positions or its projection on one direction and recover the shape of the trapping potential $U(x)$. In cases where the shape of the trap is not well approximated by a harmonic potential, possibly holographic optical tweezers, it would be useful to determine the shape of the trap with this method, and also compare it with the resulting power spectrum.

This method works well to describe the shape of the trapping potential only within the range of thermally sampled positions, x. However, when external forces are applied to the trapped particle, it generally experiences a larger offset from the trap center than explored in the absence of applied force. Thus the trap shape at larger displacements becomes relevant for quantitative force measurements and must be determined by other means (*e.g.* the application of a calibrated flow force [62]).

2.6 Conclusions

In this chapter I presented a description of our single beam optical tweezers instrument, and introduced the methods used to calibrate the trap stiffness. We built the optical tweezers based on custom optical elements, and incorporated micropipette and flow control. For quantitative measurement of displacement and force exerted on the trapped bead, we use a video tracking method and forward-scattered light position measurement. The relation between optical force and bead displacement, or the trap stiffness, is calibrated by multiple methods. The equipartition theorem gives a quick measure of the trap stiffness, but in a unit related to the photodetector, thus requiring prior calibration of the photodetector sensitivity. This procedure is done by moving a bead in the trapping area using the piezoelectric stage. The dependence on bead size of this calibration may introduce a systematic error when calculating the trap stiffness in real units. I then presented another more sophisticated method. The power spectrum of the trapped bead's thermal motion gives information related to the trap stiffness, and therefore can be used for trap calibration. The hydrodynamic effects of a moving bead in fluid are also included in the model. By doing this, not only is the precision improved (to 0.5%), but also information about the bead size is obtained (5% precision). However, the corner frequency, the key parameter for calibrating the trap, is related to the trap stiffness by the bead size. Therefore, to make full use of the high precision of the corner frequency determination, it is necessary to measure the bead size or its diffusion constant more precisely. A hybrid method aiming for solving this problem has been proposed in [49]. I have repeated this experiment and found a good linear relation between the driving amplitude and the bead's response, suggesting a potential high-precision calibration method. However, the bead size result does not agree with the hydrodynamical values, and has a systematic inconsistency between the two directions. Further improvements in instrumentation are required.

Chapter 3

Brownian motion in a modulated trap

In the previous chapter, I discussed the dynamics of an optically trapped particle in a stationary trap and a spatially modulated trap. It is shown in Equation (2.43) that the bead's response to external perturbation follows a Lorentzian, indicating that the high frequency component of the motion is attenuated by the viscous fluid and the low-frequency motion is confined by the trap. In the temporal domain, Joykutty *et al.* reported an observation of parametric resonance of the trapped particle when the intensity of the trap was modulated [51]. Their observation suggested the surprising result that the inertial effect in an overdamped system was significant. I repeated this experiment but could not reproduce the parametric resonance. Also, from analysis of the modulated system, I derived a relation between modulation frequency and the variance of the bead's motion. This relation is confirmed by experiment.

3.1 Calculation of variance

Here, I introduce the equation of motion of an optically trapped bead in a temporally modulated harmonic potential. I focus on the particle's position variance and discuss its behavior in both high- and low- modulation frequency limits. The central results in this analysis are based on the equations of motion for the time evolution of the position variance for a Brownian particle in a parametrically modulated harmonic trap with arbitrary damping. Those equations were first derived by Zerbe *et al.* [55]. Here, we give an alternate derivation for the overdamped case and discuss briefly how to extend it to the more general arbitrary-

damping case.

For a trapped particle subjected to a sinusoidally modulated trap stiffness, the overdamped equation of motion (2.11) becomes

$$\gamma_0 \dot{x} + \kappa[1 + \epsilon \cos(\Omega t + \phi)]x = \sqrt{2k_B T \gamma_0}\, \xi(t)\,, \tag{3.1}$$

where ϵ is the modulation depth, Ω the modulation frequency and ϕ the initial phase. In experiments, this initial phase is usually unknown and evenly distributed between 0 and 2π. In our linear dissipative system (3.1), information about the initial conditions decays exponentially and thus does not affect the asymptotic behaviour; since we are only interested in the latter, the initial phase can be set to 0.

To solve for the position, I first scale t using the corner frequency $t' = 2\pi f_c t$. The overdamped equation of motion (3.1) then becomes

$$\dot{x} + [1 + \epsilon \cos(\frac{\Omega}{2\pi f_c} t')]x = \sqrt{\frac{2D}{2\pi f_c}}\xi(t')\,. \tag{3.2}$$

The equivalent stochastic differential equation is

$$dx = -[1 + \epsilon \cos(\frac{\Omega}{2\pi f_c} t')]x dt' + \sqrt{\frac{2D}{2\pi f_c}} dw(t')\,, \tag{3.3}$$

where $w(t')$ is a Wiener process with $\langle w(t) \rangle = 0$ [72]. Following the derivation of Itō's lemma [72, 73],

$$\begin{aligned} d(x^2) &= 2x\, dx + (dx)^2 \\ &= -2[1 + \epsilon \cos(\frac{\Omega}{2\pi f_c} t')]x^2 dt' + 2\sqrt{\frac{2D}{2\pi f_c}} x dw(t') + \frac{2D}{2\pi f_c} dw^2(t') \\ &= 2\left[-[1 + \epsilon \cos(\frac{\Omega}{2\pi f_c} t')]x^2 + \frac{D}{2\pi f_c}\right] dt' + 2\sqrt{\frac{2D}{2\pi f_c}} x dw(t')\,, \end{aligned} \tag{3.4}$$

since $dw^2 = dt'$ and I neglect terms of higher order than dt'. Also, for a continuous function

$f(x)$ of $x(t')$,

$$\begin{aligned} d\langle f(x)\rangle &= \int dx_1 f(x_1) p(x_1, t+dt) - \int dx_0 f(x_0) p(x_0, t) \\ &= \int dx_1 f(x_1) \int dx_0 p(x_1, t+dt|x_0, t) p(x_0, t) - \int dx_0 f(x_0) p(x_0, t) \\ &= \int dx_0 p(x_0, t) \left(\int dx_1 f(x_1) p(x_1, t+dt|x_0, t) - f(x_0) \right) \\ &= \int dx_0 p(x_0, t) \langle df(x)\rangle|_{x=x_0} \\ &= \langle df(x)\rangle. \end{aligned} \tag{3.5}$$

Here $p(x,t)$ is the probability density of the stochastic variable $x(t)$, and $p(x_1, t_1|x_0, t_0)$ is the conditional probability density for the system to evolve from state (x_0, t_0) to (x_1, t_1).

Thus, since $\langle x\rangle = 0$, and $\langle x(t')dw(t')\rangle = 0$, the position variance $\sigma_{xx} = \langle x^2\rangle$ is

$$\begin{aligned} d\sigma_{xx}(t') &= d\langle x^2(t')\rangle \\ &= \langle dx^2(t')\rangle \\ &= 2\left[-[1 + \epsilon\cos(\frac{\Omega}{2\pi f_c}t')]\langle x^2(t')\rangle + \frac{D}{2\pi f_c} \right] dt' , \end{aligned} \tag{3.6}$$

or

$$2\pi f_c \, \dot{\sigma}_{xx}(t') = 2\left[D - \frac{\kappa}{\gamma_0}\left[1 + \epsilon\cos(\frac{\Omega}{2\pi f_c}t') \right] \sigma_{xx} \right] . \tag{3.7}$$

In the general second-order stochastic system (*i.e.*, including the inertial term neglected in (3.1)),

$$\frac{m\kappa}{\gamma_0^2}\ddot{x} + \dot{x} + \left[1 + \epsilon\cos(\frac{\Omega}{2\pi f_c}t') \right] x = \sqrt{\frac{2D}{2\pi f_c}}\xi(t') , \tag{3.8}$$

where the factor $4\zeta^2 \equiv \gamma_0^2/m\kappa = (\omega_0/2\pi f_c)^2$ is used to characterize the strength of damping, and $\omega_0 = \sqrt{m/\kappa}$ is the natural frequency of the system. In our case, this squared damping factor is $\mathcal{O}(10^2)$. To determine the variance of the motion of the trapped bead, we can use the covariance matrix [55],

$$\sigma(t) = \begin{pmatrix} \sigma_{xx}(t) & \sigma_{xv}(t) \\ \sigma_{xv}(t) & \sigma_{vv}(t) \end{pmatrix} = \begin{pmatrix} \langle x^2\rangle - \langle x\rangle^2 & \langle xv\rangle - \langle x\rangle\langle v\rangle \\ \langle xv\rangle - \langle x\rangle\langle v\rangle & \langle v^2\rangle - \langle v\rangle^2 \end{pmatrix} . \tag{3.9}$$

Following a derivation similar to that used for the first-order system, one can show that the stochastic system described in (3.8) leads to the following dynamical equations for the

elements of the covariance matrix [55]:

$$\begin{aligned} \dot{\sigma}_{xx} &= 2\sigma_{xv}; \\ \dot{\sigma}_{xv} &= -\frac{\gamma_0^2}{m\kappa}\left[\sigma_{xv} + [1+\epsilon\cos(\frac{\Omega}{2\pi f_c}t')]\sigma_{xx}\right] + \sigma_{vv}; \\ \dot{\sigma}_{vv} &= -2\frac{\gamma_0^2}{m\kappa}\left[\sigma_{vv} + [1+\epsilon\cos(\frac{\Omega}{2\pi f_c}t')]\sigma_{xv}\right] + \frac{2D\gamma_0^2}{m^2\,(2\pi f_c)^3}\,. \end{aligned} \tag{3.10}$$

In the overdamped limit, $\gamma_0^2/(m\kappa) = (\omega_0/2\pi f_c)^2 \gg 1$, and the time scales of σ_{xv} and σ_{vv} are much faster than σ_{xx}. I therefore eliminate them adiabatically by setting $\dot{\sigma}_{xv} = \dot{\sigma}_{vv} = 0$ and easily recover (3.7).

Returning to the overdamped case, Equation (3.7) in unscaled units (real time) becomes

$$\dot{\sigma}_{xx}(t) = 2\left[\frac{k_BT}{\gamma_0} - \frac{\kappa}{\gamma_0}\,(1+\epsilon\cos\Omega t)\,\sigma_{xx}\right]. \tag{3.11}$$

When $\epsilon \ll 1$, the approximate solution of (3.11) gives a Lorentzian form for the variance as a function of modulation frequency [52].

I now examine the behaviour of (3.11) in the limit of high and low Ω for insight into how the frequency of modulation affects the position variance of the trapped bead. The solution of (3.11) can be written in integral form as

$$\sigma_{xx}(t) = \frac{k_BT}{\kappa} - \frac{2k_BT\epsilon}{\gamma_0}e^{-\frac{2\kappa}{\gamma_0}[t+\frac{\epsilon}{\Omega}\sin\Omega t]}\int_0^t e^{\frac{2\kappa}{\gamma_0}[\tau+\frac{\epsilon}{\Omega}\sin\Omega\tau]}\cos\Omega\tau d\tau\,, \tag{3.12}$$

where I have assumed that initially σ_{xx} has the equilibrium value given by the equipartition theorem, k_BT/κ.

In the limit of fast modulation $\Omega \gg 1$, (3.12) is Taylor expanded to

$$\sigma_{xx}(t) = \frac{k_BT}{\kappa} - \frac{2k_BT\epsilon}{\gamma_0\Omega}\,(\sin\Omega t) + \mathcal{O}(\frac{1}{\Omega^2})\,. \tag{3.13}$$

Thus, for fast modulation, the asymptotic spatial variance oscillates around the equilibrium value sinusoidally with a magnitude proportional to $1/\Omega$. The solution approaches the equilibrium value as Ω increases:

$$\sigma_{xx|\Omega\to\infty} = \frac{k_BT}{\kappa}\,, \tag{3.14}$$

This system, with corner frequency f_c, can respond only to perturbations slower than f_c. The trapped bead experiences only the average trap stiffness in this case of high-frequency modulation.

In the limit of slow modulation $\Omega \ll 1$, $\dot{\sigma}_{xx}$ in (3.11) vanishes adiabatically, and

$$\sigma_{xx|\Omega\ll 1} = \frac{k_B T}{\kappa\left(1+\epsilon\cos\Omega t\right)}. \tag{3.15}$$

The result in (3.15) can be obtained intuitively by noting that if the trap stiffness is modulated as $\kappa\left(1+\epsilon\cos\Omega t\right)$, with a modulation frequency much lower than the corner frequency, the motion of the bead is always governed by the instantaneous trap stiffness. The average variance over one period is

$$\langle\sigma_{xx}\rangle_{\Omega\ll 1} = \frac{k_B T}{\kappa}\frac{\Omega}{2\pi}\int_0^{2\pi/\Omega}\frac{dt}{1+\epsilon\cos\Omega t} = \frac{k_B T}{\kappa\sqrt{1-\epsilon^2}}. \tag{3.16}$$

Compared with the cases of fast or no modulation, the variance increases for slow modulation with an experimentally detectable factor, $1/\sqrt{1-\epsilon^2}$. The transition between these two limiting cases (3.14) and (3.16) is governed by f_c, since the overdamped system has only one timescale, $1/f_c$ [52].

I solved (3.11) numerically to show the relation between position variance and modulation frequency for the overdamped system (Figure 3.1, solid lines). In the limit of slow modulation, the variance is increased relative to a trap of constant stiffness κ by a factor of $1/\sqrt{1-\epsilon^2}$. As the modulation frequency increases beyond the corner frequency, the variance approaches that of an unmodulated trap because the system is not able to respond faster than the corner frequency f_c.

To further test the analysis, I also performed Monte Carlo simulations of (3.1), using parameters to match the experiments described in the next section. Figure 3.1 (closed symbols) demonstrates that the relation between modulation frequency and Brownian motion from the simulations agrees with the numerical solution to (3.11).

In the more general case including inertial effects, fluctuations are described by a symmetric 2-by-2 covariance matrix for σ_{xx}, σ_{xv} and σ_{vv}, where v represents velocity. The time evolution of the covariance matrix was derived in Equation (3.10) and in [55]. Here, I integrate the solution numerically to show that parametric resonance [54] vanishes when the stochastic system goes from under- to overdamped (Figure 3.2). The value of the damping factor $\zeta \equiv \gamma_0/2\sqrt{m\kappa} = \omega_0/4\pi f_c$ is set to several values near 1 and the asymptotic stationary solution of the covariance matrix (3.10) is solved and averaged over one period. The result shows a damped parametric resonance peak vanishing as the damping factor

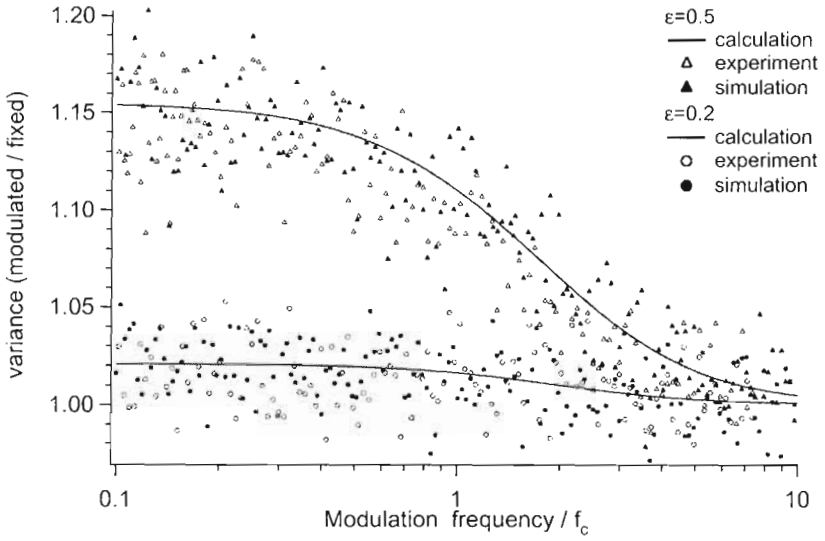

Figure 3.1: Position variance plotted as a function of modulation frequency Ω, at two different modulation depths, $\epsilon = 0.2$ (circles) and 0.5 (triangles). The predictions from (3.11) are shown as solid lines, with Monte Carlo simulations (closed symbols) and experimental data (open symbols) superposed. The transition from low- to high-frequency limit ($k_BT/(\kappa\sqrt{1-\epsilon^2})$ to k_BT/κ) occurs at the corner frequency, f_c.

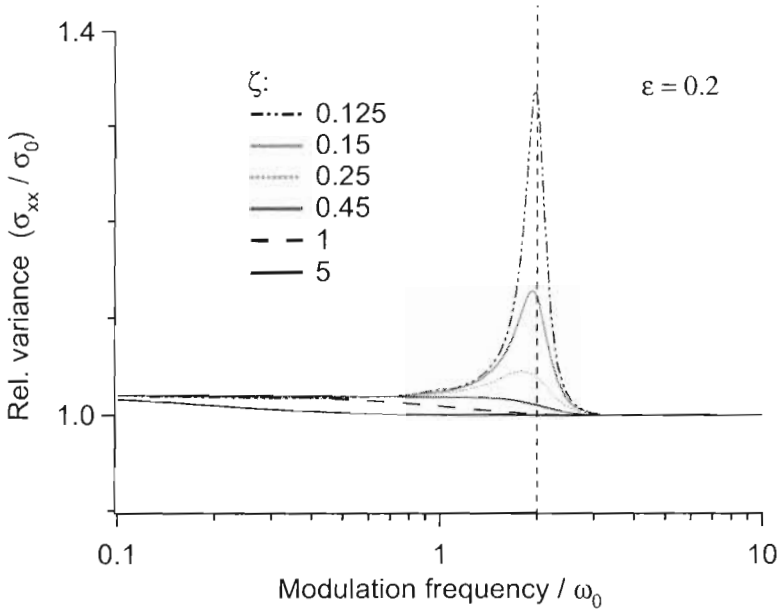

Figure 3.2: Numerical solution to (3.10) for the position variance in the vicinity of critical damping, for a modulation depth $\epsilon = 0.2$. The variances are relative to the unmodulated equilibrium value. The damping factor $\zeta \equiv \gamma_0/2\sqrt{m\kappa}$ is used to characterize the damping strength. In the low damping regime, a parametric resonance peak is shown clearly near $2\omega_0$. As the damping increases beyond critical damping, the resonance peak quickly vanishes.

increases. In a typical optical tweezers setup where a 2.1-μm-diameter polystyrene bead is trapped by a 100 pN/μm optical trap, the dimensionless damping factor is $\mathcal{O}(10)$. An increase in the variance near $2\omega_0$ due to parametric modulation is thus not expected.

To summarize: from the stochastic equation of motion, I have derived the dynamics of the covariance matrix and calculated the variance of the position signal. The variance has different behaviour in the low- and high-modulation- frequency limits, leading to a transition in variance near the corner frequency.

3.2 Experimental approach

To experimentally test the above theoretical results, I trapped a polystyrene bead in an optical tweezers instrument and modulated the trap strength. I determined the variance as a function of modulation frequency and compared the result with the theory.

3.2.1 Experimental Setup

The experimental setup for a temporally modulated trap (Figure 3.3) is similar to that is described in Section 2.3. In order to change the trap stiffness, I directly modulated the driving current with a laser driver (Melles Griot 06DLD203A) via a computer-controlled function generater (Stanford Research Systems DS345). Because the trapping laser is modulated and because the output signal from the photodetector and its associated amplifier depends on the intensity of the light, I added a weaker, unmodulated laser (660 nm, 30 mW diode laser from Circulase and Blue Sky Research) and a separate position-sensitive photodetector (UDT Sensors DL-10) to perform position detection in these experiments.

In these experiments, I modulated the laser current about a mean value that corresponded to a characteristic bead corner frequency near 400 Hz. This frequency was in the middle (logarithmically) of a range defined, on the low end, by drifts limiting sampling lengths to $\lesssim 0.1$ s and, on the high end, by the bandwidth of the laser modulation driver (10 kHz). Using the intensity of the trapping laser as read by the photodetector, I set the chosen modulation depths to 1% accuracy.

3.2.2 Laser pointing instability

In addition to modulating the laser intensity, varying the current also led to a $\sim$100 nm shift in the central position of the optical trap depending on the intensity. The discussions in Section 2.4 suggest that when the spatial modulation is significant, a sharp peak in the power spectrum is expected at the modulation frequency Ω. To first order, if the position changes linearly with laser intensity and if both position and intensity change sinusoidally with time[1], the position variance will increase as ϵ^2. Thus, the increase in variance due to

[1]This simplification is coarse since the measurement of the bead's position as a function of trapping laser power shows multiple plateaux in addition to an overall shift in the vertical direction (relative to the optical

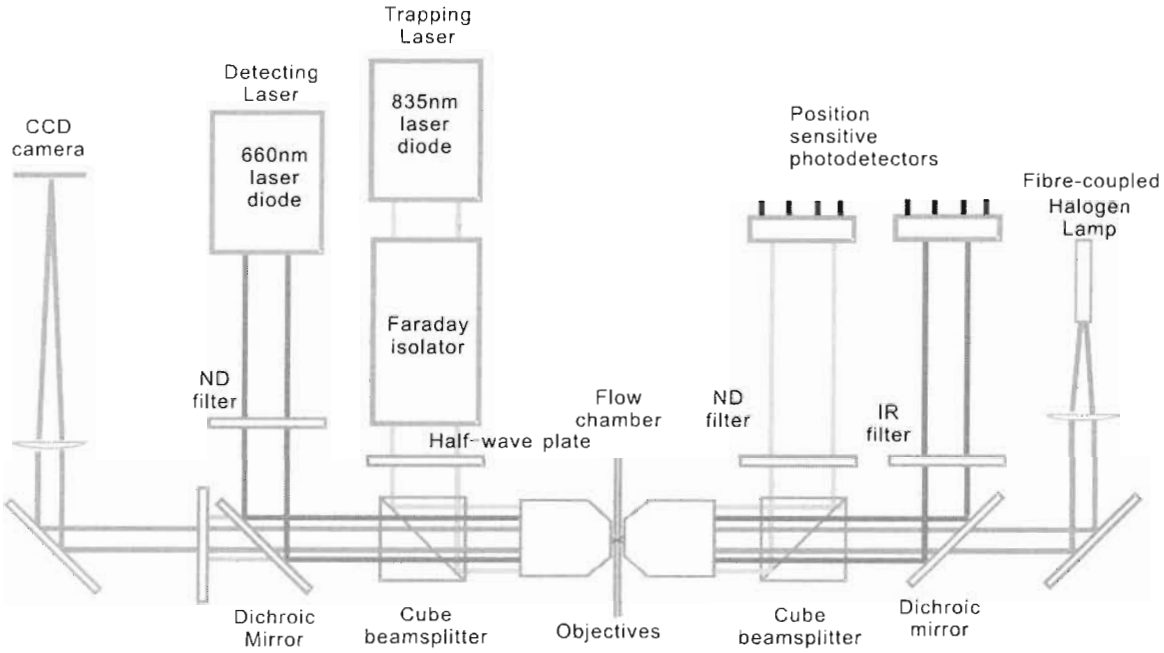

Figure 3.3: The optical trapping setup used in position-variance measurements. This setup is built on the stationary trap described in Section 2.2 and Figure (2.2). In addition to the main infrared trapping laser, a red laser measures the position of a trapped bead using a second position-sensitive photodetector (PSD). The trapping-laser current is controlled by a laser driver driven by a computer-controlled function generator.

spatial modulation resembles that due to temporal modulation (both are $\mathcal{O}(\epsilon^2)$); however, the effects are easily distinguished in the power spectrum, since spatial modulation implies a peak at Ω while intensity modulation gives no peak, in the overdamped case.

Although this gave a large spurious contribution to the position variance, I realized that the spatial modulation was always along one direction. Because of the linearity of the equation of motion (3.1), the effect of this spatial modulation was minimized by measuring position fluctuations along the orthogonal direction. To do this, I rotated the photodetector so that the spurious motion was along one axis of the detector (the vertical axis in Figure 3.4). This decoupling procedure eliminated the spatial modulation along the orthogonal axis and allowed me to study the system in this one dimension. This method is valid only if the system dynamics are linear and the pointing instability is one dimensional, which were both true here.

3.2.3 Frequency scan sequence

Since the bead may be knocked out of the trap by another bead, it is hard to predict the lifetime of a trapped bead. The concentration of beads in solution is adjusted to a value ($\sim 10^7 ml^{-1}$) such that one single bead should be able to stay in the trap stably for the time scale of 10 minutes. In these experiments, the modulation frequency is scanned in a way that the modulation frequencies sampled evenly span the whole range of interest no matter when the experiment has to stop. Given an upper and lower bound of this frequency range, in the first round the modulation frequency is the midpoint of this range, while the following rounds modulate at the midpoints between the frequencies of the previous rounds. Therefore the n^{th} round has 2^{n-1} frequencies that are probed.

3.2.4 Instrument drift and compensation

The corner frequency was determined from the power-spectrum method to be 393 ± 3 Hz (Figure 3.5), and the modulation frequency was chosen to range from 30 Hz to 3 kHz. For each modulation frequency, I recorded a series of 100 position-time measurements, each

table). The nonlinear pointing direction-power relation will add discrete harmonics of the basic modulation frequency to the resulting power spectrum of the bead's motion.

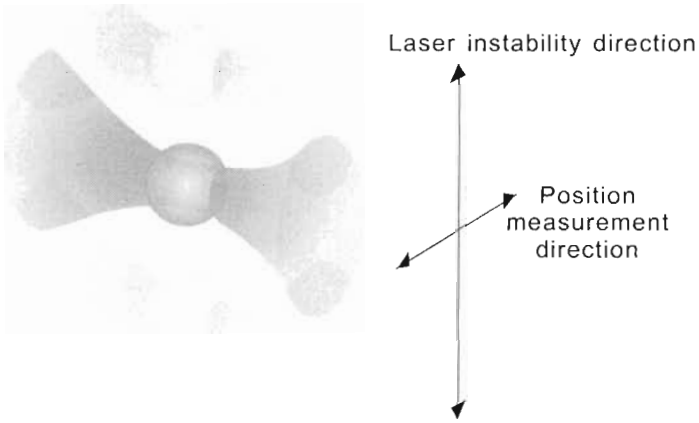

Figure 3.4: Sketch showing the (exaggerated) effect of the pointing instability of the trapping laser diode. The vertical motion creates a periodic force that modulates the vertical position of the particle. Because of the linearity of the equations of motion, displacements in the orthogonal, horizontal direction are unaffected. I thus rotated the position detector to align its vertical axis with the modulated motion of the bead and recorded positions along the orthogonal direction.

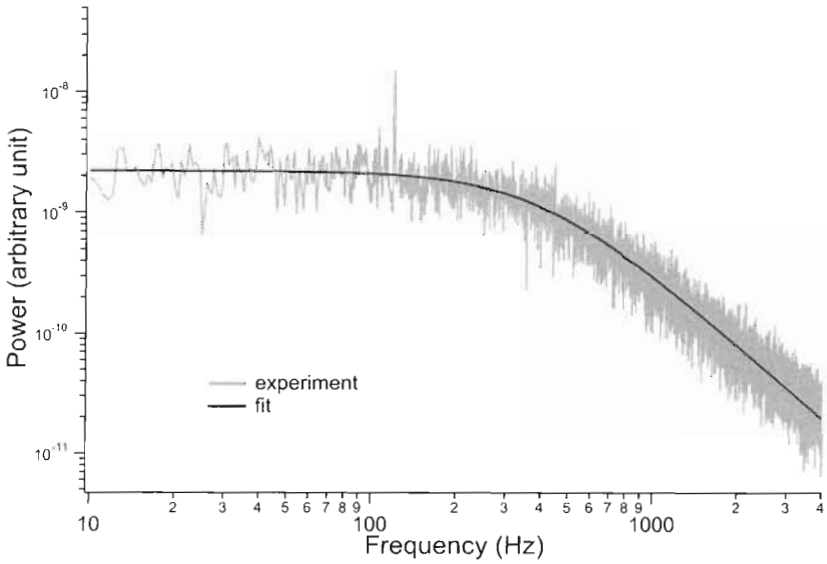

Figure 3.5: Power spectrum of the trapped bead (2.1 μm, polystyrene), as measured by the main trapping laser with unmodulated, constant power ($\approx$ 30 mW at the trap). Solid line is a fit to a modified Lorentzian (Section 2.2.4 and Equation (2.27)) and gives a corner frequency of 393 ± 3 Hz. The sharp peak at 120 Hz is from the mechanical vibration of the objective lens mounts and was filtered out prior to fitting. The power spectrum obtained using the red detecting laser gave the same corner frequency (data not shown).

sampled at 30 kHz for 0.1 s. After each series of measurements at a given modulation frequency, I recorded an identical control series without modulation.

I took the control measurements because of the low-frequency drifts in measured positions. The position variance arises from three primary sources in these measurements: the intrinsic Brownian motion of the trapped particle (B), the increase in variance due to modulation (M), and experimental "ambient" noise (A) such as drift of the optical path and, more importantly here, hops between laser modes in the detection laser. The true increase of variance due to trap intensity modulation is estimated by comparing the variance with modulation to a variance calculated from averaged data from an unmodulated trap taken immediately before and afterward.

For comparison with theory, we require the ratio $(B + M)/B$. The experimental ratio of modulated to unmodulated variance does not completely compensate for the effect of noise. This is because the ambient noise and laser drift are additive to the Brownian motion of the trapped bead. I approximate the desired ratio

$$\frac{B+M}{B} = 1 + \frac{M}{B}$$

by the direct ratio between the measurements

$$\frac{B+M+A}{B+A} = 1 + \frac{M}{B+A} \approx 1 + \frac{M}{B} - \frac{AM}{B^2}\,.$$

The first two terms recover the desired ratio, and the last term vanishes under the limit $A << B$, which is true in our setup, independent of the strength of the modulation. This is justified by the fact that the power spectrum is well fit by Lorentzian.

3.2.5 Data filtering and results

I calculated the variances of each 100 modulated and control position-time series for each modulation frequency and median filtered these 100 variances. Because variances are always positive, measurement errors are always biased to positive values, and occasional large external noise (other beads flowing by the beam path, large mechanical vibrations etc.) can overwhelm the Brownian motion signal. A median filter thus gives a better estimate of the true relative variance than does an averaging filter. Figure 3.1 shows the normalized experimental variance obtained as a function of modulation frequency. The numerical

simulation data and theoretical calculations, which use the same parameters as in the experiments, are also included. All results are consistent and show that at low frequencies, the relative variance asymptotically approaches $1/\sqrt{1-\epsilon^2}$, with a transition frequency equal to the corner frequency. Notice that the scatter in the variance measurements is consistent with the scatter in the Monte Carlo simulations, showing that I have correctly modeled not only the physics of the trapped bead but also the statistics of the experimental measurements.

3.2.6 Null test for the parametric resonance

Since these experiments were undertaken to examine the claim of parametric resonance in optical tweezers [51], I tried to reproduce these results. While Joykutty *et al.* modulated their laser intensity with an acousto-optic modulator, I directly varied the current, and hence power output, of the laser diode. Laser power was adjusted to give a similar trap strength to that used in [51], and I probed beads of the same size. For my experiments, the trapping power was reduced such that the corner frequency f_c was $49.4Hz$ for a $3.17\mu m$ polystyrene bead. The trap stiffness κ was therefore $9.27pN/\mu m$, and the natural frequency $f_0 = \omega_0/2\pi = 3.75kHz$. I scanned the modulation frequency in a range from $5kHz$ to $10kHz$ and measured the variance of the position from a 10 s time series sampled at 16 kHz. I observed no evidence for a resonance peak in this range (Figure 3.6).

3.3 Discussion

The focus of this chapter was to determine how the position variance of an optically trapped object is affected by a temporally modulated trap intensity. We found that at low modulation frequencies, the variance with modulation is higher than without modulation by a factor of $1/\sqrt{1-\epsilon^2}$, where ϵ is the depth of modulation. In the high-frequency limit, the variance is governed by the time-averaged stiffness of the optical trap and equals the variance without modulation. The transition between these two limiting cases occurs on the timescale of viscous relaxation, which is related to the corner frequency. I showed theoretically, numerically and experimentally that the transition frequency indeed occurs around the corner frequency for different modulation depths.

In principle, the dependence of the variance on modulation frequency could be used to

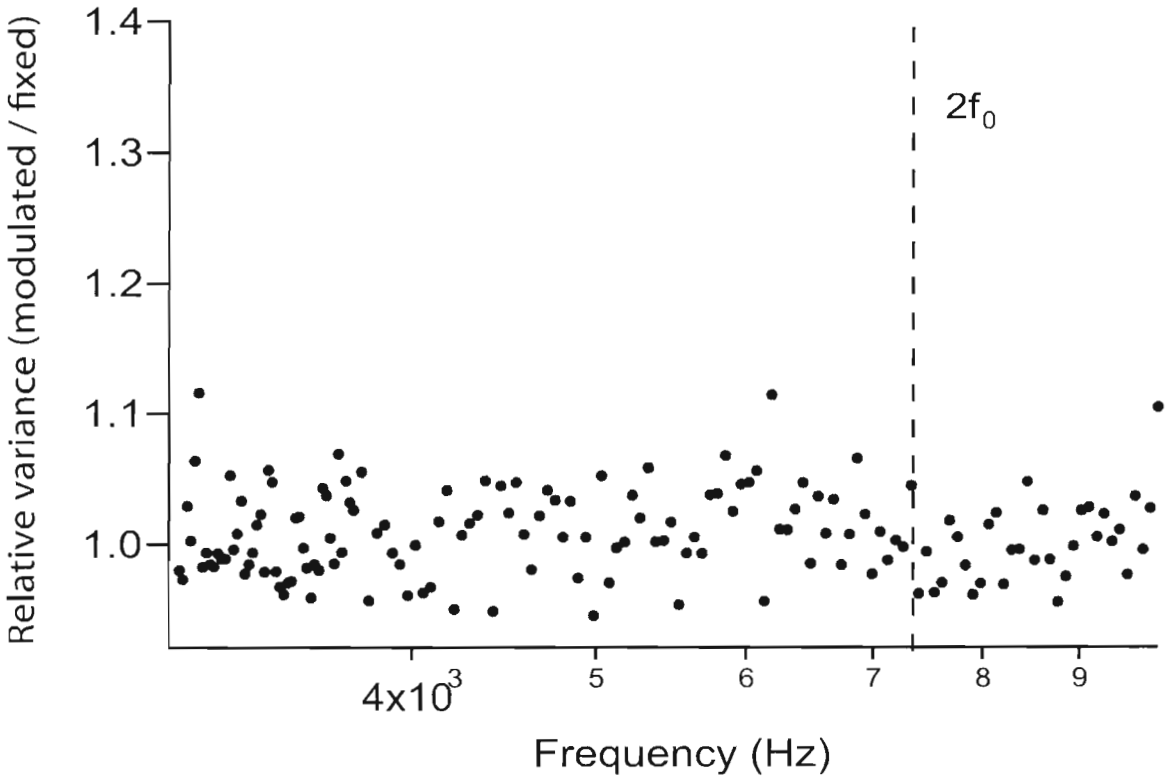

Figure 3.6: Null test for parametric resonance in the overdamped optical trap. This experiment was the repeat of Joykutty *et al.*'s experiment where parametric resonance was claimed to be observed at twice the natural frequency. Our experimental result of no parametric peak confirms the theoretical prediction that parametric resonance is not expected in an overdamped system.

calibrate an optical trap. Earlier work by Joykutty *et al.* noted a peak in the variance as a function of modulation, which they interpreted as a resulting from parametric resonance [51]. If true, this would enable a precise determination of the trap stiffness, as the observed peak is sharp. However, the theoretical arguments presented here and in [52] imply that no such peak is expected in a highly overdamped system. In addition, a careful scan of the variance near the expected frequency ($2\omega_0$) in our system showed no such peak (Figure 3.6). The result of Joykutty *et al.* is thus due to other unknown causes. Nonetheless, the observed relations between variance and modulation frequency are characterized by the trap stiffness (Figure 3.1), and thus experimentally determining this relation should enable determination of the trap stiffness. However, the absence of an analytical form for the variance-modulation relation, the long sampling time and experimental subtleties make it hard to obtain an accurate and convenient corner frequency measurement. The power-spectrum-analysis method discussed in Chapter 2, which uses all the information in the position signal, remains the best calibration method.

Although the dynamics in the overdamped regime are less rich than in an underdamped system [56, 57, 58], the frequency dependence of the measured variance nonetheless has important implications for experimental design. Because there is only one time scale in overdamped systems, the corner frequency also sets the timescale for modulation in instruments such as time-sharing optical tweezers [48]. When controlled by an acousto-optic deflector, the modulation frequency is usually on the scale of kHz or higher, depending on the size of the modulator and number of traps [48]. Effectively, the trapped bead acts as a low-pass filter for the modulation. So long as the modulation frequency is much higher than the corner frequency, the variance is independent of the specific waveform of modulation. In such an application, the effect of modulation can be neglected, and each trap can be treated as having a constant trapping strength given by the time-averaged intensity at each trap. Here, it is also valid to treat the force-displacement relation as linear. When controlled by a rotating mirror, by contrast, the modulation is much slower [23, 31, 74, 75], and the position variance of isolated trapped beads can be time dependent, with a time-averaged value higher than when trapped by a constant-power trap. In this case, the optical trap should only be used as a tool to move objects. Since the force-displacement relation depends on the details of modulation (frequency, duty cycle etc.), quantitative measurements will be highly susceptible to systematic errors. As the modulation amplitude increases close

to $\epsilon = 1$ (full on/off modulation), the relation between variance and modulation frequency becomes increasingly ill fit by a Lorentzian, with the variance diverging at low frequencies; however, the high-frequency behaviour is independent of modulation depth, converging to variance of a time-averaged trap at frequencies greater than $10f_c$. Therefore, for quantitative analysis, the modulation frequency should be at least an order of magnitude above the corner frequency.

In many biophysical applications, optical tweezers are used to probe the mechanical properties of biological systems. In such applications, the trapped bead is in contact with or tethered to a soft molecule or material. This can result in a decrease of the viscous relaxation time of the bead because of the elasticity of the attached molecule, effectively increasing the corner frequency [48]. In such a case, a time-sharing trap that gives reliable quantitative results on isolated beads may nonetheless give systematic errors when applied to force measurements on materials. Additionally, in this type of experiment, an external force applied to the trapped bead results in a displacement from the trap centre, and thus modulation of the trap stiffness will induce an oscillation of the bead's position. Under certain conditions this oscillation amplitude can exceed the Brownian motion, which has implications when characterizing force-dependent systems such as molecular motors. Therefore, care must be taken when using time-sharing traps for force-sensitive studies.

Another reason to modulate the trap stiffness in optical tweezers is to actively control the trap stiffness in order to create a constant-force trap or a position controller [4]. The constant-force trap (force clamp) is useful in biophysical and biochemical studies, in which a controllable force load can be used to probe systems such as molecular motors, nucleic acids and protein folding, and to measure statistics in near- and non-equilibrium systems [9]. Besides active intensity modulation, other ways to create a force clamp include laminar fluid flow [46, 47, 76, 77], active position feedback [42, 78], scanning the trap centre with a changing trap strength [43], and taking advantage of the anharmonic trapping potential [79]. Most of these other techniques require expensive modulators such as acousto-optic deflectors or high-resolution positioning stages, whereas intensity modulation can be performed cheaply by modulating the current of a laser diode. Also, when used for position control, although closed-loop feedback does not increase the signal-to-noise ratio of force measurements, physically reducing the Brownian motion can nonetheless be useful. For example, for studies on short molecules, reducing the Brownian motion can decrease unwanted con-

tributions from interactions between closely spaced beads. Also, since many theoretical arguments are more simply framed in terms of a constant-force constraint, comparisons between experiment and theory are simplified by measurements in which the force is held fixed [80]. The frequency response of the variance discussed in our study suggests that the closed-loop feedback bandwidth must exceed the corner frequency in order to effectively control the signal or force in the face of perturbations due to thermal noise.

3.4 Conclusion

In a typical optical tweezers setup, the corner frequency, proportional to the trap stiffness, is the relevant time scale for the system. I observed experimentally that if the laser intensity is modulated sinusoidally, the variance of the position of the trapped object increases by a factor of $1/\sqrt{1-\epsilon^2}$ in the low-modulation-frequency limit, and the transition takes place around the corner frequency. In principle, this variance-modulation frequency dependence could be used to calibrate an optical trap; however, the standard power spectrum method is better, being more accurate, faster and requiring less hardware. On the other hand, I have shown that low modulation frequencies do lead to detectable increases in the position variance, and I have confirmed the expected form of the increase. Such variances can lead to systematic errors in force measurements from time-varying traps, and I have given criteria for avoiding such effects.

Chapter 4

Conclusions

The work in the first part of this thesis implements the calibration procedure described in [50] on our optical tweezers instrument. The technical details on how to calibrate the optical tweezers using the thermal motion of a trapped bead are presented in Chapter 2. The equipartition theorem results in a quick determination of the trap stiffness, but the conversion factor from the position detector signal to real displacement must be measured separately, and this method is susceptible to external noise of all kinds. A more advanced approach decomposes the motion into the frequency domain and analyzes the shape of the power spectrum density. The Lorentzian shape from the basic equation of motion does not describe the motion very well when high precision (better than 1%) is required. After taking hydrodynamic effects and other experimental factors into account, the refined model agrees with the experimental data well, giving at least 0.5% precision for the determination of the corner frequency. The hydrodynamic model also gives an estimate to the bead size, but since hydrodynamic effects occur at much higher frequency than the corner frequency, the precision in the bead size (5%) does not match that in the corner frequency. In the determination of the trap stiffness from the corner frequency, the bead size is a key parameter. In principle, a hybrid method that combines the analysis of the thermal motion and the response of the bead's motion to an external spatial perturbation solves this problem. The preliminary data I have obtained show the possibility of obtaining the diffusion constant and the bead size from this method. Further experiments still need to be done for this method to be practical in our instrument. Despite the fact that the power spectrum method only calibrates the trap stiffness within the small spatial range sampled by the bead because

of thermal fluctuations, it is overall a fast and precise calibration method compared with other methods.

The effects of temporal modulation on the trapping potential are discussed in theory and the experiments confirm the results in Chapter 3. The central result of this chapter is the relation between the position variance of the trapped bead and the modulation frequency. From the basic equation of motion of the trapped bead, the dynamics of the position variance is derived for the general case with inertia and for its simplification in the overdamped case, and is calculated numerically for both cases. When the underdamped condition is satisfied, the variance has a resonance peak at twice the modulation frequency, known as parametric resonance. When the damping increases to the overdamped regime, the resonance behaviour vanishes. This result is expected since parametric resonance is caused by the phase correlation between the motion of the bead and the external modulation of the potential, and this correlation is lost when the damping time scale of the system is shorter than one period of the modulation. In the overdamped case, instead of the natural frequency, the typical time scale of the system becomes the corner frequency. It is shown in theory that the variance has a transition at the corner frequency, from the high-frequency limit where the bead only experiences the average trapping intensity, to the low-frequency limit where the bead tracks the instantaneous trapping strength. This result was confirmed in experiments. I used a two-laser setup to trap a bead and detect its position separately, and the modulation was achieved by changing the laser driving current. The transition of variance was observed, and the observation agreed well with the theoretical prediction and numerical simulation.

In addition to improving the shaking-stage method to further refine the calibration of the optical trap, improvements to the theoretical model of the trapped bead are potentially useful. The boundary effect is known to modify the theoretical trap stiffness by up to 2% for the experimental geometries of our instrument. If the trap stiffness can be determined to this precision, for example using the hybrid method, including boundary effects in the model will become necessary. Another factor that affects the power spectrum is the shape of the trapping potential. An alternative characterization method for the trap stiffness and determination of the trap potential shape for small displacements are presented in Chapter 2.

Appendix A

Fourier transform

A.1 Definitions

In this thesis, the Fourier transform for a continuous measurement $x(t)$ with finite length T_{msr} is defined as

$$\tilde{x}_k \equiv \int_0^{T_{msr}} x(t) e^{-2\pi i f_k t} dt \,, f_k \equiv k/T_{msr} \,, k \in \mathbb{Z} \,. \tag{A.1}$$

In the discrete version with an evenly sampled time series $\{(t_j = j\Delta t, x_j) | j = 0, ..., N-1\}$,

$$\tilde{x}_k \equiv \Delta t \sum_{j=0}^{N-1} x_j e^{-2\pi i f_k t_j} \,, f_k \equiv k/T_{msr} \,, k \in \mathbb{Z} \,. \tag{A.2}$$

It can be shown that $\tilde{x}_k$ is a periodic function with period N for discretely sampled data (similar to the derivation in Section A.2). When $x(t)$ or x_j is real, $\tilde{x}_k$ satisfies:

$$\tilde{x}_k = \tilde{x}^*_{-k} \,.$$

The *two-sided* power spectrum density is defined as

$$P[x](f_k) \equiv |\tilde{x}_k|^2 / T_{msr} \,. \tag{A.3}$$

In this thesis, Fourier transform and power spectrum (density) are defined over the range $[-f_{Nyq}, f_{Nyq})$ or $[0, f_s)$ (*i.e.* double sided), but only the data in $[0, f_{Nyq})$ is used in the analysis because of the two properties listed above.

A.2 Aliasing

Consider a harmonic component $x(t) = e^{2\pi i f_0 t + \phi_0}$ with an arbitrary frequency f_0 and initial phase ϕ_0 that is sampled discretely at $t = 0, 1/f_s, ..., (N-1)/f_s$ at sampling frequency f_s. Its Fourier transform is

$$\begin{aligned} \tilde{x}_k &= \Delta t \sum_{j=0}^{N-1} e^{2\pi i f_0 t_j + \phi_0} e^{-2\pi i f_k t_j} \\ &= \Delta t \sum_{j=0}^{N-1} e^{2\pi i f_0 t_j + \phi_0 + 2\pi i (nj)} e^{-2\pi i f_k t_j} \\ &= \Delta t \sum_{j=0}^{N-1} e^{2\pi i (f_0 + n f_s) t_j + \phi_0} e^{-2\pi i f_k t_j} , \end{aligned} \tag{A.4}$$

if $n \in \mathbb{Z}$. This result shows that in a discrete Fourier transform, harmonic components that differ by a multiple of the sampling frequency contribute to the same frequency in the Fourier transform. In applications, because the Fourier transform is conventionally defined on either $[-f_{Nyq}, f_{Nyq})$ or $[0, f_s)$, higher frequency signals will "fold" into this range. An anti-aliasing filter is commonly used to remove high-frequency components and therefore prevent these distortions due to aliasing.

A.3 Leakage

In the discrete Fourier transform, let T_{msr} be the total length of the sample in time, N the number of samples, and therefore the sampling rate $f_s = N/T_{msr}$. For a single harmonic oscillation $e^{2\pi i f t}$ with frequency f, its k^{th} Fourier component is

$$\begin{aligned} \tilde{x}_k &= \sum_{j=0}^{N-1} e^{2\pi i f \frac{j T_{msr}}{N}} e^{-2\pi i \frac{jk}{N}} \\ &= \sum_{j=0}^{N-1} e^{2\pi i (T_{msr} f - k) \frac{j}{N}} \\ &= \begin{cases} N & : \quad T_{msr} f = k \\ \frac{1 - e^{2\pi i (T_{msr} f - k)}}{1 - e^{2\pi i (T_{msr} f - k)/N}} & : \quad T_{msr} f \neq k \end{cases} . \end{aligned} \tag{A.5}$$

In the case where the sample time T_{msr} is an integer multiple of the signal period $1/f$, *i.e.* $T_{msr}f$ is an integer, the Fourier transform has only one non-zero value at f_k.

A.4 Fourier transform of Gaussian white noise

The expected value of the power spectrum density of Gaussian white noise can be derived from the stochastic version of the Wiener-Khintchine theorem [64]. Let $\xi(t)$ be Gaussian white noise satisfying Equation (2.8), then

$$\langle|\tilde{\xi}|^2\rangle = \int_0^{T_{msr}} \langle\xi(0)\xi(t)\rangle e^{-2\pi i f t} dt \tag{A.6}$$

$$= 1\,, \tag{A.7}$$

because of (2.8).

The distribution of the power spectrum density is less straightforward. An intuitive picture to see the distribution of the Fourier transform of the Gaussian white noise is that the transform kernel $e^{-2\pi i f t}$ is modulated by a random number with Gaussian distribution, and therefore the Fourier integration is analogous to the central-limit theorem on the complex plane, resulting in a stochastic variable with Gaussian-distributed magnitude and an evenly distributed phase. The probability density distribution of $|\tilde{\xi}|^2$ is then exponential.

The relation between the Fourier transform and the characteristic function of a stochastic variable gives a more rigorous derivation. Also see [81] for more discussions on the effect of finite sample length and windowing on the distribution of the transform.

Appendix B

Frequency response of the anti-aliasing filter

The combined frequency response of the anti-aliasing filter and A/D converter in series is measured by feeding a sinusoidal signal into the filter and fitting the readout from the A/D converter with a sinusoidal function. The ratio of the output to input magnitudes gives the gain of the filter-DAQ system. To cover the full frequency range probed in the experiments, the frequency range is divided into four decades with some overlap. The gain is fit to a polynomial (Figure B.1) which is then used in the estimate of the physical power spectrum calculation in the actual fitting procedure.

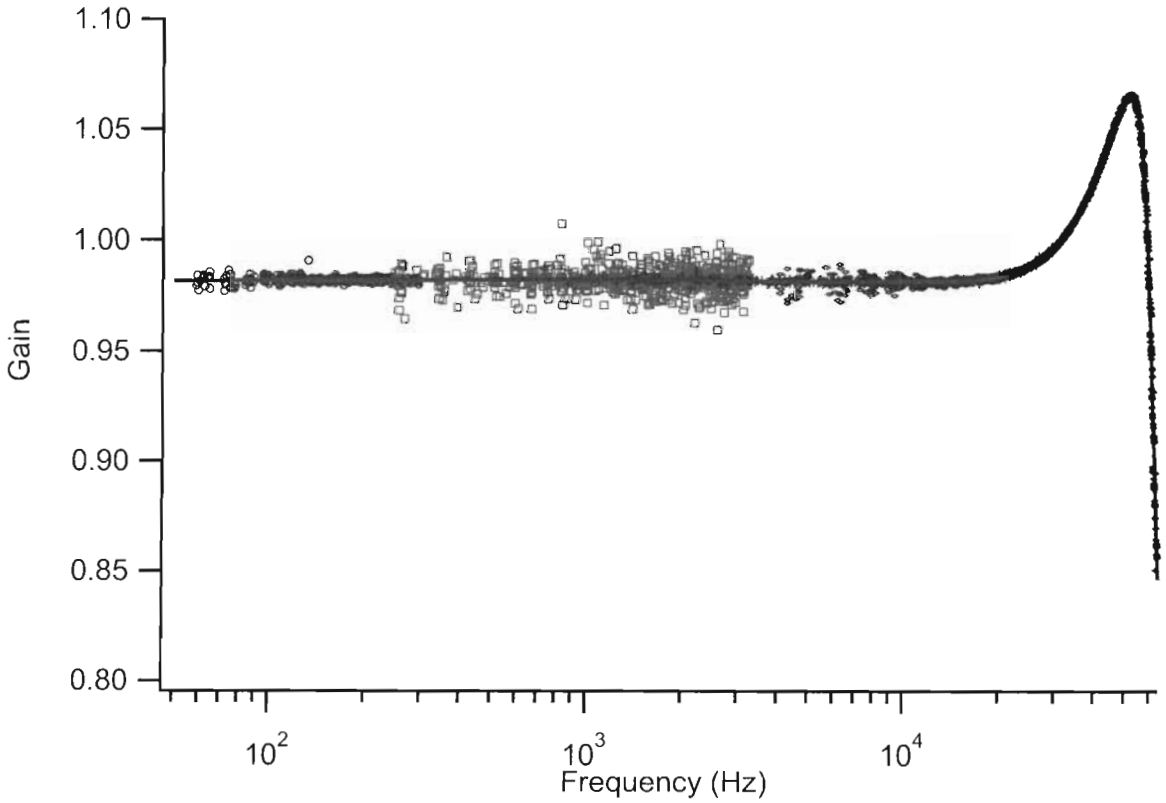

Figure B.1: The response of the low-pass filter used for anti-aliasing. The full frequency range is acquired in four separate decades with overlaps (shown in four symbols), and is fit with a 11th-order polynomial as shown in the solid line and Table B. This polynomial is subsequently used in the calculation of the physical spectrum for spectrum fitting. From the response, it is clear that the overshoot-attenuation above 10 kHz have to be taken into account for an accurate estimate of the power spectrum.

Table B.1: The coefficients of the polynomial fit to the response of the anti-aliasing filter.

power	coefficient for response of x channel	coefficient for response of y channel
0	0.981632	0.981371
1	1.292079×10^{-6}	2.208835×10^{-7}
2	-9.046740×10^{-10}	-1.988370×10^{-10}
3	2.377822×10^{-13}	5.456703×10^{-14}
4	-3.242748×10^{-17}	-7.976361×10^{-18}
5	2.595445×10^{-21}	6.811878×10^{-22}
6	-1.295773×10^{-25}	-3.585045×10^{-26}
7	4.153858×10^{-30}	1.202686×10^{-30}
8	-8.546862×10^{-35}	-2.576523×10^{-35}
9	1.090499×10^{-39}	3.409170×10^{-40}
10	-7.849222×10^{-45}	-2.536046×10^{-45}
11	2.434174×10^{-50}	8.098874×10^{-51}

Appendix C

Noise of the system

Since the work in this thesis focuses on the power spectrum and the position variance of a trapped particle, the system noise and measurement noise are important parameters, and are relatively straightforward to characterize in the frequency domain. Different noise sources generate noise at very different ranges, and different treatments are applied to reduce these noise contributions.

C.1 High-frequency electronics noise

50 kHz is very commonly used in switching power supplies, and this noise contributes to electrical contamination of signals via the power supply line directly and radiation. Although 50 kHz is above our frequency range of interest, aliasing of its harmonics will generate a series of sharp spikes below the Nyquist frequency, some occurring in the power spectrum fitting range, if an anti-aliasing filter is not used. It is not critical for the fitting since this noise appears in the form of sharp spikes at predictable frequencies and can be excluded from the fit. However, proper experimental treatment will effectively reduce the contributions of this electronic noise to measurements.

To remove the high-frequency noise from the power supply line, I used a linear power supply (BCM-15/100, Datel Systems, Inc.) instead of a switching power supply for the PSD pre-amplifier. Two 6-volt batteries are used for the anti-aliasing filter. The radiation noise is removed by applying proper shielding to the electronic elements. Shielded cables are selected for signal transfer, and the PSD and its pre-amplifier are protected in aluminum

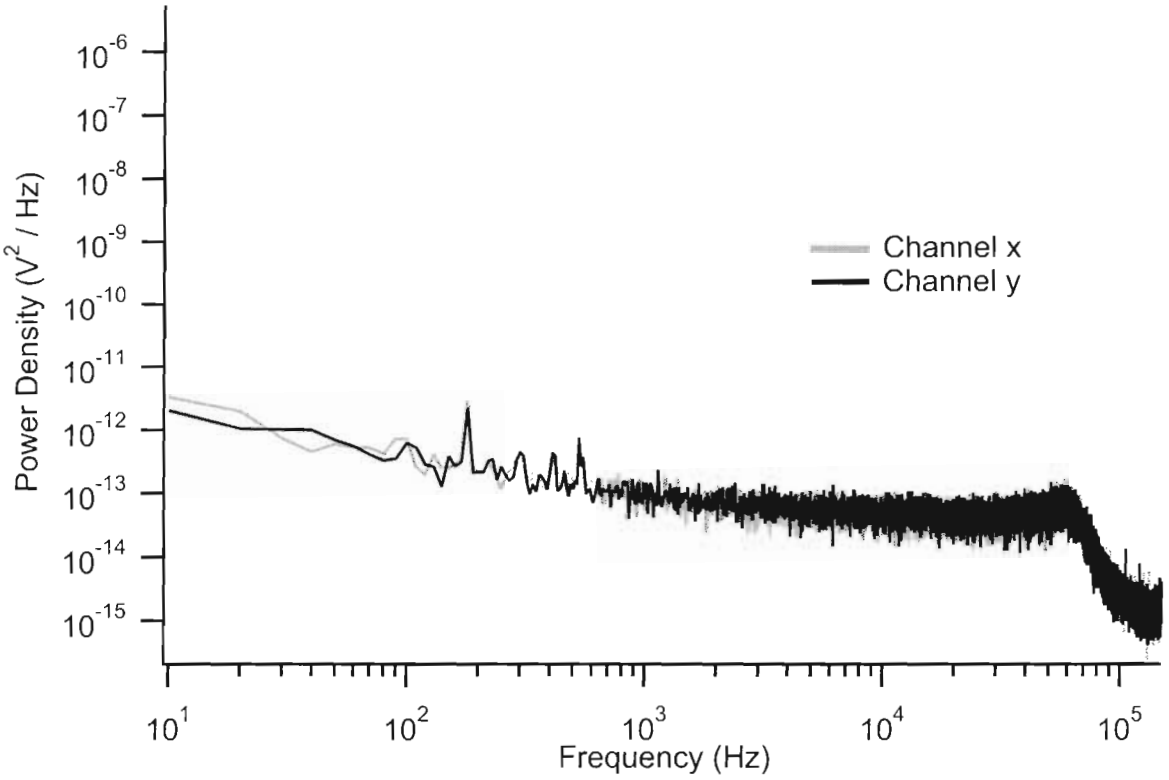

Figure C.1: Dark noise power spectrum. The PSD signal is recorded in the dark to measure the electronic noise. The noise floor is generated by the anti-aliasing filter and is higher than the A/D converter digitization noise (data not shown), but much lower than the signal, *i.e.* the thermal noise of the trapped bead (10^{-9} V^2/Hz at 10 Hz, see Figure 2.7) within the fitting range.

boxes. This reduces all high-frequency noise essentially to the noise floor of the anti-aliasing filter (Figure C.1).

C.2 Vibration of objectives

In the mid-frequency range, the major contribution of noise in our measurement is from the mechanical vibration of the microscope objectives, with frequencies ranging from 100 Hz to 1 kHz. The objectives are each mounted on a translational stage by a top plate, which introduces vibrational motion. The magnitude of these vibrations is larger in the vertical

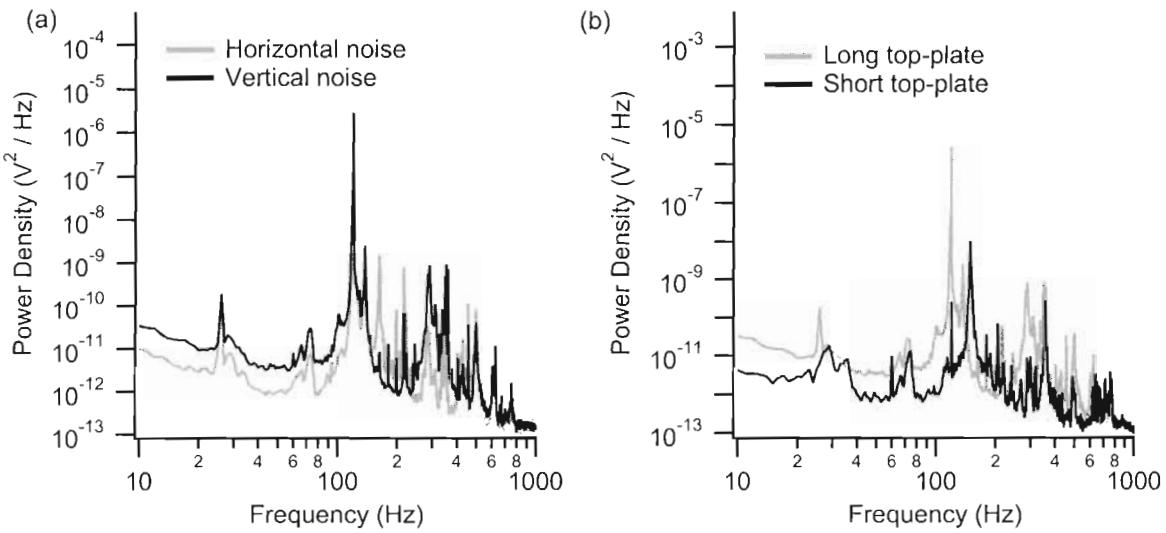

Figure C.2: Noise due to the mechanical vibration of objectives. (a) Noise power spectrum for the long top plates in two directions. Blue: vertical, Red: horizontal. Because of the asymmetry of the setup, vibrations in vertical direction have a larger magnitude than in the horizontal direction. (b) Comparison between the vertical noise from long and short top plates. Dark (blue): long plate; light (red): short plate. The noise magnitude is reduced for the short top plate compared to the long one, and also the resonance frequencies are shifted.

direction than in the horizontal direction. I characterize the vibration noise by measuring the position signal of the laser going through the two objectives, but with no bead trapped. Figure C.2 shows different noise arising from the vibration of top plates of two different sizes (6.0 cm$\times$ 6.0 cm, and 6.0 cm$\times$ 11.0 cm respectively).

Limited by the horizontal design of the instrument layout, it is hard to effectively reduce the magnitude of the mechanical vibration of the objective. The noise level is mostly one order of magnitude below the typical thermal noise of the trapped bead, but the strongest resonance peak at 120 Hz is often seen in the power spectrum above the Brownian motion. In all the fitting procedures, values within [118, 122] Hz are omitted from the analysis.

C.3 Air-density fluctuation and optical stability

At low frequency (<1 Hz), the noise is dominated by air-density fluctuations and instrument drift. To reduce the air-current flow, we built an epoxy glass chamber enclosing all the optical elements. Even though the room temperature is regulated within 0.2°C, from the result of video tracking and PSD signal of a stationary bead, typical drift can exceed 100 nm in the time scale of 100 seconds (Figure C.3). The frequency at which the drift exceeds the Brownian motion of the trapped particle determines the lower bandwidth limit of typically $\sim$1 Hz for measurement of a power spectrum.

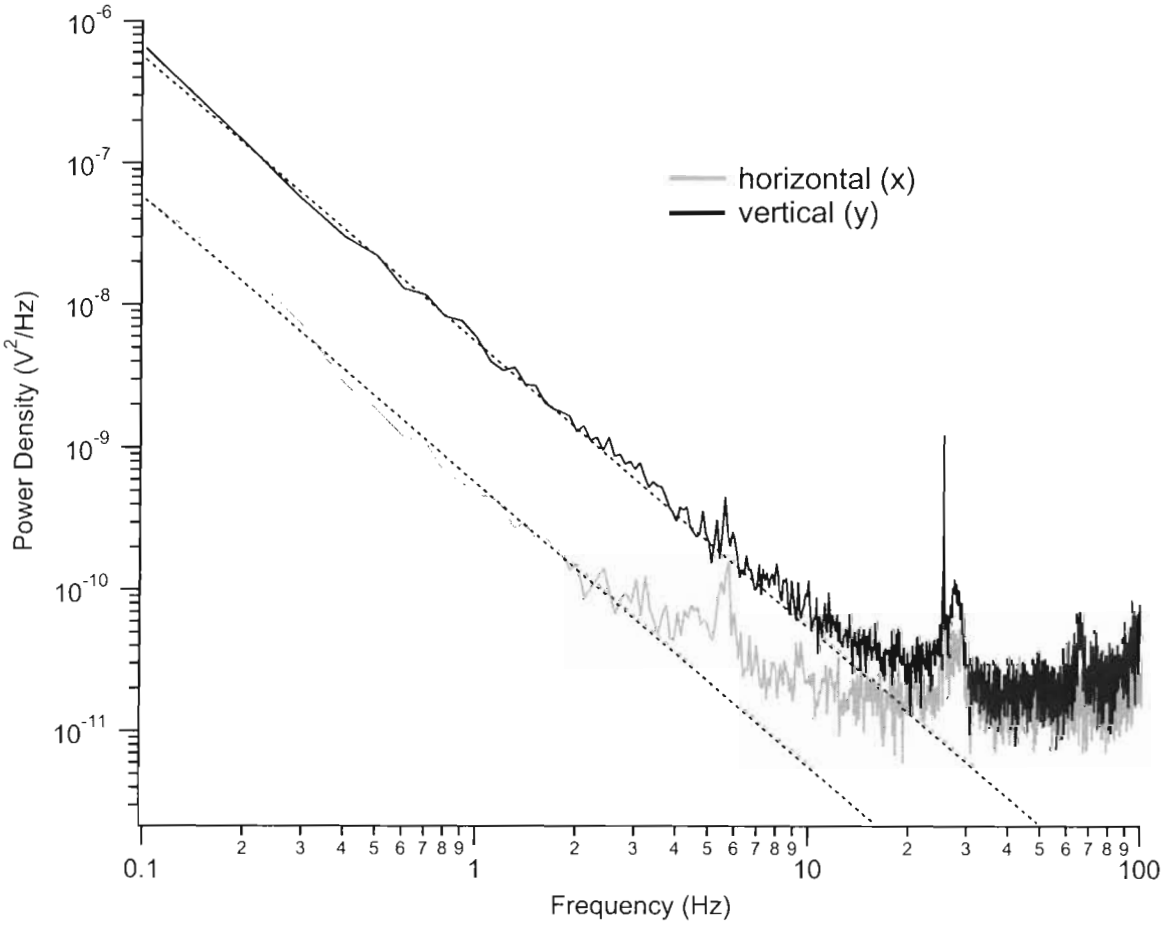

Figure C.3: The low-frequency noise due to drift in the instrument. The slope of the two dashed lines is -2. The different magnitudes in the vertical and horizontal directions suggest that this noise is primarily caused by the drift of the microscope objective mounts.

Appendix D

Optical alignment

The alignment of the tweezers follows the steps listed below.

D.1 Trapping

- Rough height adjustments: All optical paths are on a plane parallel to the optical table, therefore all elements should be roughly at the same height, especially the laser head and microscope objective stages.

- Place the laser head at the proper place on the optical table; adjust the Faraday isolator according to its manual to allow maximum transmission and minimum back reflection. Insert the half-wave plate, adjust its orientation to obtain the maximum transmission.

- Place the cube beam splitter (BS) in the beam path; Rotate the half-wave plate so that the cube BS reflection is maximized; adjust the angle of the cube BS so that the reflected beam is parallel to the optical table and a row of holes. Use the PSD mounted on a rail to record the location of the beam path.

- Insert both microscope objectives and a flow chamber with water (and pipette, optional), then adjust the positions of the two objectives so that the throughput beam is roughly collimated and the chamber is roughly in the middle of the objectives.

- Fine tune the positions of the objectives so that the throughput beam follows the exact beam path (as detected by the PSD) as before the objectives are inserted.
- Trap a bead, then check the power spectrum of the trapped bead.

D.2 Imaging and illumination

- Remove the position detector. Add the illuminating light source to the condenser side.
- Insert the proper short-pass filter, imaging lens and camera at the trapping laser side, and adjust the position of the imaging lens to obtain the image of the trapped bead. For locating the position of the trap, see Philip Johnson's thesis [62].
- Adjust the position of the illumination light source so that the bead is illuminated symmetrically. All additional illumination optical elements should be treated the same way.
- Insert one convex lens (L1) between the condenser objective and the illumination light to give a real image of the light source between this lens and the condenser objective.
- Insert an iris (condenser diaphragm) at the position of the image of the light source.
- Insert a second convex lens (L2) between the condenser diaphragm and the condenser objective to give a second real image near the condenser objective.
- Fine tune the position of the second lens so that opening and closing the condenser lens results in a uniform change in the intensity of the image.

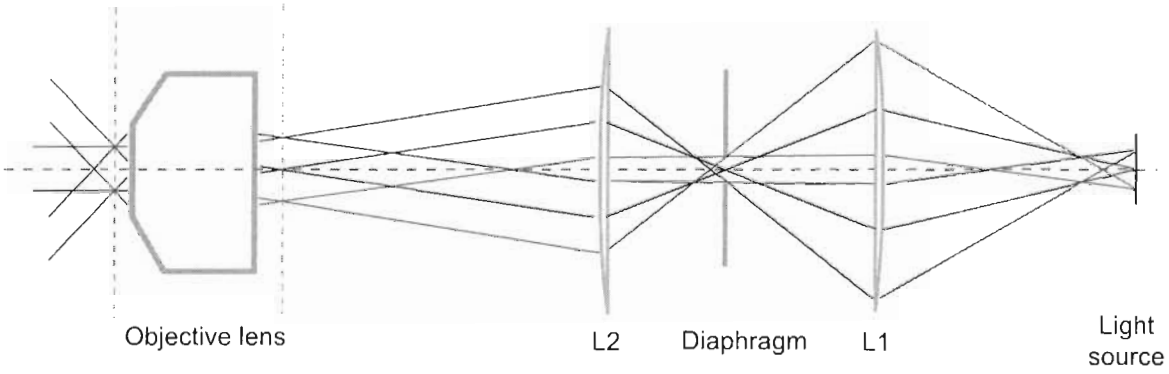

Figure D.1: Ray diagram of the illumination optical path. The light coming out of the illumination source is imaged on the diaphragm plane by the first lens L1, and the diaphragm is then imaged on the back focal plane of the microscope objective by the second lens L2. The imaging plane in the flow chamber should coincide with the trapping plane.

Bibliography

[1] A. Ashkin, J. M. Dziedzic, J. E. Bjorkholm, and S. Chu. Observation of a single-beam gradient force optical trap for dielectric particles. *Opt. Lett.*, 11:288–290, 1986.

[2] M. J. Lang and S. M. Block. Resource letter: LBOT-1: Laser-based optical tweezers. *Amer. J. Phys.*, 71:201–215, 2003.

[3] S. B. Smith, Y. J. Cui, and C. Bustamante. Overstretching B-DNA: The elastic response of individual double-stranded and single-stranded DNA molecules. *Science*, 271:795–799, 1996.

[4] M. D. Wang, H. Yin, R. Landick, J. Gelles, and S. M. Block. Stretching DNA with optical tweezers. *Biophys. J.*, 72:1335–1346, 1997.

[5] C. Cecconi, E. A. Shank, C. Bustamante, and S. Marqusee. Direct observation of the three-state folding of a single protein molecule. *Science*, 309:2057–2060, 2005.

[6] B. Onoa, S. Dumont, J. Liphardt, S. B. Smith, I. Tinoco Jr., and C. Bustamante. Identifying kinetic barriers to mechanical unfolding of the T. thermophila ribozyme. *Science*, 299:1892–1895, 2003.

[7] M.T. Woodside, W.M. Behnke-Parks, K. Larizadeh, K. Travers, D. Hershlag, and S.M Block. Nanomechanical measurements of the sequence-dependent folding landscapes of single nucleic acid hairpins. *Proc. Natl. Acad. Sci.*, 103:6190–6195, 2005.

[8] S. M. Block. Real engines of creation. *Nature*, 386:217–219, 1997.

[9] C. Bustamante, Y. R. Chemla, N. R. Forde, and D. Izhaky. Mechanical processes in biochemistry. *Annu. Rev. Biochem.*, 73:705–748, 2004.

[10] Y. Cui and C. Bustamante. Pulling a single chromatin fiber reveals the forces that maintain its higher-order structure. *Proc. Natl. Acad. Sci.*, 97:127–132, 2000.

[11] M. L. Bennink, S. H. Leuba, G. H. Leno, J. Zlatanova, B. G. de Grooth, and J. Greve. Unfolding individual nucleosomes by stretching single chromatin fibers with optical tweezers. *Nat. Struct. Biol.*, 8:606–610, 2001.

[12] B. D. Brower-Toland, C. L. Smit, R. C. Yeh, J. T. Lis, C. L. Peterson, and M. D. Wang. Mechanical disruption of individual nucleosomes reveals a reversible multistage release of DNA. *Proc. Natl. Acad. Sci.*, 99:1960–1965, 2002.

[13] S. M. Block, C. L. Asbury, J. W. Shaevitz, and M. J. Lang. Probing the kinesin reaction cycle with a 2D optical force clamp. *Proc. Natl. Acad. Sci.*, 100:2351–2356, 2003.

[14] T. Yanagida, K. Kitamura, H. Tanaka, A. H. Iwane, and S. Esaki. Single molecule analysis of the actomysin motor. *Curr. Opin. Cell. Biol.*, 12:20–25, 2000.

[15] J. E. Molloy, J. E. Burns, J. Kendrick-Jones, R. T. Tregear, and D. C. S. White. Movement and force produced by a single myosin head. *Nature*, 378:209–212, 1995.

[16] S. M. Block, L. S. Goldstein, and B. J. Schnapp. Bead movement by kinesin molecules studied with optical tweezers. *Nature*, 348:348–352, 1990.

[17] Y. Inoue, Y. Y. Toyoshima, A. H. Iwane, S. Morimoto, H. Higuchi, and T. Yanagida. Movements of truncated kinesin fragments with a short or an artificial flexible neck. *Proc. Natl. Acad. Sci.*, 94:7275–7280, 1997.

[18] G.J.L. Wuite, S. B. Smith, M. Young, D. Keller, and C. Bustamante. Single molecule studies of the effect of template tension on T7 DNA polymerase activity. *Nature*, 404:103–106, 2000.

[19] B. Maier, D. Bensimon, and V. Croquette. Replication by a single DNA polymerase of a stretched single-stranded DNA. *Proc. Natl. Acad. Sci.*, 97:12002–12007, 2000.

[20] W. Singer, M. Frick, T. Haller, S. Bernet, M. Ritsch-Marte, and P. Dietl. Mechanical forces impeding exocytotic surfactant release revealed by optical tweezers. *Biophys. J.*, 84:1344–1351, 2003.

[21] A. Ashkin and J. M. Dziedzic. Internal cell manipulation using infrared laser traps. *Proc. Natl. Acad. Sci.*, 86:7914–7918, 1989.

[22] J. Guck, R. Ananthakrishnan, T. J. Moon, C. C. Cunningham, and J. Käs. Optical deformability of soft biological dielectrics. *Phys. Rev. Lett.*, 84:5451–5454, 2000.

[23] G. Lenormand, S. Hénon, A. Richert, J. Siméon, and F. Gallet. Direct measurement of the area expansion and share moduli of the human red blood cell membrane skeleton. *Biophys. J.*, 81:43–56, 2001.

[24] J Guck, R Ananthakrishnan, C. C. Cunningham, and J. Käs. Stretching biological cells with light. *J. Phys.: Condens. Matter*, 14:4843–4856, 2002.

[25] K. Lin, J. C. Crocker, A. C. Zeri, and A. G. Yodh. Colloidal interactions in suspensions of rods. *Phys. Rev. Lett.*, 87:088301, 2001.

[26] S. Lee and D. G. Grier. Holographic microscopy of holographically trapped three-dimensional structures. *Opt. Ex.*, 15:1505–1512, 2007.

[27] X. C. Yao and A. Castro. Optical trapping microfabrication with electrophoretically delivered particles inside glass capillaries. *Opt. Lett.*, 28:1335–1337, 2003.

[28] S. C. Chapin, V. Germain, and E. R. Dufresne. Automated trapping, assembly, and sorting with holographic optical tweezers. *Opt. Ex.*, 14:13095–13100, 2006.

[29] E. Schonbrun, R. Piestun, P. Jordan, J. Cooper, K. Wulff, J. Courtial, and M. Padgett. 3D interferometric optical tweezers using a single spatial light modulator. *Opt. Ex.*, 13:3777–3786, 2005.

[30] C. Mio, T. Gong, A. Terray, and D. W. M. Marr. Design of a scanning laser optical trap for multiparticle manipulation. *Rev. Sci. Inst.*, 71:2196–2200, 2000.

[31] K. Visscher, G. J. Brakenhoff, and J. J. Krol. Micromanipulation by "multiple" optical traps created by a single fast scanning trap integrated with the bilateral confocal scanning laser microscope. *Cytometry*, 14:105–114, 1993.

[32] A. La Porta and M. D. Wang. Optical torque wrench: Angular trapping, rotation, and torque detection of quartz microparticles. *Phys. Rev. Lett.*, 92:190801, 2004.

[33] J. E. Curtis, B. A. Koss, and D. G. Grier. Dynamic holographic optical tweezers. *Opt. Comm.*, 207:169–175, 2002.

[34] J. E. Curtis and D. G. Grier. Structure of optical vortices. *Phys. Rev. Lett.*, 90:133901, 2003.

[35] K. Ladavac and D. G. Grier. Microoptomechanical pumps assembled and driven by holographic optical vortex arrays. *Opt. Ex.*, 12:1144–1149, 2004.

[36] A. Hoffmann, G. Meyer zu Hörste, G. Pilarczyk, S. Monajembashi, V. Uhl, and K. O. Greulich. Optical tweezers for confocal microscopy. *Appl. Phys.* B, 71:747–753, 2000.

[37] G. V. Shivashankar and A. Libchaber. Single DNA molecule grafting and manipulation using a combined atomic force microscope and an optical tweezers. *Appl. Phys. Lett*, 71:3727–3729, 1997.

[38] M. W. Berns, Y. Tadir, H. Liang, and B. Tromberg. Laser scissors and tweezers. *Methods Cell Biol.*, 55:71–79, 1998.

[39] C. S. Buer, P. J. Weathers, and G. A. Swartzlander, Jr. Changes in hechtian strands in cold-hardened cells measured by optical microsurgery. *Plant Physiol.*, 122:1365–1377, 2000.

[40] B. Abou and F. Gallet. Probing a nonequilibrium Einstein relation in an aging colloidal glass. *Phys. Rev. Lett.*, 93:160603, 2004.

[41] R. M. Simmons, J. T. Finer, S. Chu, and J. A. Spudich. Quantitative measurements of force and displacement using an optical trap. *Biophys. J.*, 70:1813–1822, 1996.

[42] M. J. Lang, C. L. Asbury, J. W. Shaevitz, and S. M. Block. An automated two-dimensional optical force clamp for single molecule studies. *Biophys. J.*, 83:491–501, 2002.

[43] R. Nambiar and J-C Meiners. Fast position measurements with scanning line optical tweezers. *Opt. Lett.*, 27:836–838, 2002.

[44] K. C. Neuman and S. M. Block. Optical trapping. *Rev. Sci. Inst.*, 75:2787–2809, 2004.

[45] A. Rohrbach. Stiffness of optical traps: Quantitative agreement between experiment and electromagnetic theory. *Phys. Rev. Lett.*, 95:168102, 2005.

[46] S. C. Kuo and M. P. Sheetz. Force of single kinesin molecules measured with optical tweezers. *Science*, 260:232–234, 1993.

[47] G. J. Wuite, R. J. Davenport, A. Rappaport, and C. Bustamante. An integrated laser trap/flow control video microscope for the study of single biomolecules. *Biophys. J.*, 79:1155–1167, 2000.

[48] K. Visscher, S. P. Gross, and S. M. Block. Construction of multiple-beam optical traps with nanometer-resolution position sensing. *IEEE J. Sel. Top. Quant. Electronics*, 2:1066–1076, 1996.

[49] S. F. Tólic-Nørrelykke, E. Schäffer, J. Howard, F. S. Pavone, F. Jülicher, and H. Flyvbjerg. Calibration of optical tweezers with positional detection in the back focal plane. *Rev. Sci. Inst.*, 77:103101, 2006.

[50] K. Berg-Sørensen and H. Flyvbjerg. Power spectrum analysis for optical tweezers. *Rev. Sci. Inst.*, 75:594–612, 2004.

[51] J. Joykutty, V. Mathur, V. Venkataraman, and V. Natarajan. Direct measurement of the oscillation frequency in an optical-tweezers trap by parametric excitation. *Phys. Rev. Lett.*, 95:193902, 2005.

[52] L. Pedersen and H. Flyvbjerg. Comment on "Direct measurement of the oscillation frequency in an optical-tweezers trap by parametric excitation". *Phys. Rev. Lett.*, 98:189801, 2007.

[53] Y. Deng, N. R. Forde, and J. Bechhoefer. Comment on "Direct measurement of the oscillation frequency in an optical-tweezers trap by parametric excitation". *Phys. Rev. Lett.*, 98:189802, 2007.

[54] L. D. Landau and E. M. Lifshitz. *Course of Theoretical Physics: Mechanics*. Pergamon Press, Oxford, England, 3rd edition, 1976. §27.

[55] C. Zerbe, P. Jung, and P. Hänggi. Brownian parametric oscillators. *Phys. Rev.* E, 49:3626–3635, 1994.

[56] A. Görlitz, M. Weidemüller, T. W. Hänsch, and A. Hemmerich. Observing the position spread of atomic wave packets. *Phys. Rev. Lett.*, 78:2096–2099, 1997.

[57] S. Friebel, C. D'Andrea, J. Walz, M. Weitz, and T. W. Hänsch. CO_2-laser optical lattice with cold rubidium atoms. *Phys. Rev.* A, 57:R20–R23, 1998.

[58] K. Kim, H. R. Noh, Y. H. Yeon, and W. Jhe. Observation of the Hopf bifurcation in parametrically driven trapped atoms. *Phys. Rev.* A, 68:031403, 2003.

[59] J. D. Jackson. *Classical Electrodynamics*. John Wiley & Sons, Inc., U.S.A., second edition edition, 1975. pp. 151.

[60] A. Ashkin. Forces of a single-beam gradient laser trap on a dielectric sphere in the ray optics regime. *Biophys. J.*, 61:569–582, 1992.

[61] A. Zakharian, M. Mansuripur, and J. Moloney. Radiation pressure and the distribution of electromagnetic force in dielectric media. *Opt. Ex.*, 13:2321–2336, 2005.

[62] P. J. M. Johnson. Toward single molecule DNA uptake by *Haemophilus influnzae*. Master's thesis, Simon Fraser University, 2007.

[63] E. A. Abbondanzieri, W. J. Greenleaf, J. W. Shaevitz, R. Landick, and S. M. Block. Direct observation of base-pair stepping by RNA polymerase. *Nature*, 438:460–465, 2005.

[64] P. Hänggi. and H. Thomas. Stochastic processes: Time evolution, symmetries and linear response. *Phys. Rep.*, 88:207–319, 1982.

[65] L. D. Landau and E. M. Lifshitz. *Course of Theoretical Physics: Fluid Mechnacis*. Pergamon Press, Oxford, England, 2nd edition, 1987.

[66] H. Faxén. Die Bewegung einer starren Kugel längs der Achse eines mit zäher Flüssigkeit gefüllten Rohres. *Ark. Mat. Astron. Fys.*, 17:1–28, 1923.

[67] J. Happel and H. Brenner. *Low Reynolds number hydrodynamics*. Martinus Nijhoff publishers, Dordrecht, P. O. Box 163, 3300 AD Dordrecht, The Netherlands, forth edition edition, 1986.

[68] T. Benesch and S. Yiacoumi. Brownian motion in confinement. *Phys. Rev.* E, 68:021401, 2003.

[69] E. R. Dufresne, D. Altman, and D. G. Grier. Brownian dynamics of a sphere between parallel walls. *Europhys. Lett.*, 53:264–270, 2001.

[70] K. Berg-Sørensen, E. J. G. Peterman, T. Weber, C. F. Schmidt, and H. Flyvbjerg. Power spectrum analysis for optical tweezers. II: Laser wavelength dependence of parasitic filtering, and how to achieve high bandwidth. *Rev. Sci. Inst.*, 77:063106, 2006.

[71] G. Y. Hu and R. F. O'Connell. 1/f noise: A nonlinear-generalized-Langevin-equation approach. *Phys. Rev.* B, 41:5586–5594, 1990.

[72] C. W. Gardiner. *Handbook of Stochastic Methods*. Springer Verlag, Berlin, Germany, second edition, 1985.

[73] K. Itō. On stochastic differential equations. *Mem. Amer. Math. Soc.*, 4:1–51, 1951.

[74] S. Hénon, G. Lenormand, A. Richert, and F. Gallet. A new determination of the shear modulus of the human erythrocyte membrane using optical tweezers. *Biophys. J.*, 76:1145–1151, 1999.

[75] P. J. Bronkhorst, G. J. Streekstra, J. Grimbergen, E. J. Nijhof, J. J. Sixma, and G. J. Brakenhoff. A new method to study shape recovery of red blood cells using multiple optical trapping. *Biophys. J.*, 69:1666–1673, 1995.

[76] R. J. Davenport, G. J. L. Wuite, R. Landick, and C. Bustamante. Single-molecule study of transcriptional pausing and arrest by *E. coli* RNA polymerase. *Science*, 287:2497–2500, 2000.

[77] N. R. Forde, D. Izhaky, G. R. Woodcock, G. J. L. Wuite, and C. Bustamante. Using mechanical force to probe the mechanism of pausing and arrest during continuous

elongation by *Escherichia coli* RNA polymerase. *Proc. Natl. Acad. Sci.*, 99:11682–11687, 2002.

[78] J. Liphardt, B. Onoa, S. B. Smith, I. Tinoco Jr., and C. Bustamante. Reversible unfolding of single RNA molecules by mechanical force. *Science*, 292:733–737, 2001.

[79] W. J. Greenleaf, M. T. Woodside, E. A. Abbondanzieri, and S. M. Block. Passive all-optical force clamp for high-resolution laser trapping. *Phys. Rev. Lett.*, 95:208102, 2005.

[80] D. K. Lubensky and D. R. Nelson. Single molecule statistics and the polynucleotide unzipping transition. *Phys. Rev.* E, 65:031917, 2002.

[81] D. R. Brillinger. *Time Series: Data Analysis and Theory*. Holden-Day, Inc., 500 Sansome Street, San Francisco, California, 94111, expanded edition, 1981.